Radiation damage in ferredoxin microcrystals using high intensity X-FEL beams

K. Nass, S. Hau-Riege

October 21, 2014

Disclaimer

Radiation damage in ferredoxin microcrystals using high intensity X-FEL beams

Karol Nass[a], Lutz Foucar[a], Thomas R.M. Barends[a], Elisabeth Hartmann[a], Sabine Botha[a], Robert L. Shoeman[a], R. Bruce Doak[a], Roberto Alonso-Mori[b], Andrew Aquila[c], Saša Bajt[d], Anton Barty[e], Richard Bean[e], Kenneth Beyerlein[e], H. Olof Jönsson[f], Wolfgang Kabsch[a], Stephan Kassemeyer[a], Jason E. Koglin[b], Michael Krumrey[g], Marc Messerschmidt[b1], Dimosthenis Sokaras[b], Garth J. Williams[b], Stefan Hau-Riege[h], Nicusor Timneanu[f], Carl Caleman[ef], Henry N. Chapman[ei], Sébastien Boutet[b] and Ilme Schlichting[a]*

[a]Department of Biomolecular Mechanisms, Max Planck Institute for Medical Research, Jahnstrasse 29, Heidelberg, D-69120, Germany

[b] SLAC National Accelerator Laboratory, 2575 Sand Hill Road, Menlo Park, 94025, USA

[c] European XFEL GmbH, Albert-Einstein-Ring 19, Hamburg, 22761, Germany

[d] Photon Science, DESY, Notkestr. 85, Hamburg, 22607, Germany

[e] Center for Free-Electron Laser Science, DESY, Notkestr. 85, Hamburg, 22607, Germany

[f]Department of Physics and Astronomy, Uppsala University, box 516, Uppsala, 75120, Sweden

[g] Physikalisch-Technische Bundesanstalt (PTB), Abbestraße 2-12, Berlin, 10587, Germany

[h] Lawrence Livermore National Laboratory, 7000 East Av., Livermore, 94550, USA

[i]Department of Physics, University of Hamburg, Luruper Chaussee 149, Hamburg, 22761, Germany

Correspondence email: Ilme.Schlichting@mpimf-heidelberg.mpg.de

[1]Current address: National Science Foundation BioXFEL Science and Technology Center, 140203 Buffalo, New York, USA

Abstract The femtosecond X-ray pulses provided by X-ray free-electron lasers (FELs) allow the acquisition of high resolution diffraction data from micron-sized macromolecular crystals at room temperature beyond the limitations of radiation damage imposed by conventional X-ray sources.

Serial femtosecond crystallography (SFX) offers the diffraction before destruction approach to X-ray crystallography by exposing tens of thousands of microcrystals, one at a time, in random orientations to FEL pulses. This allows three orders of magnitude higher dose per single shot and crystal than the tolerable room temperature dose limit at synchrotrons. FEL-induced atomic ionization, the ensuing thermalisation and random structural displacements in crystallized proteins result in a global loss of crystalline order that gates diffraction in a resolution-dependent fashion during the exposure. While local damage has been predicted in SFX, no high-resolution experiments were performed to date studying this issue. Proteins that contain metal cofactors are highly radiation sensitive since the degree of X-ray absorption correlates with the presence of high atomic charge number elements and X-ray energy. To explore the effects of local damage in SFX, *Clostridium* ferredoxin was used as a model system. The protein contains two [4Fe-4S] clusters that serve as sensitive probes for radiation-induced electronic and structural changes. High dose room temperature SFX datasets were collected at the Linac Coherent Light Source of ferredoxin microcrystals above and below the iron K-shell absorption edge using 80 fs pulses of ~10^{19} W/cm^2 irradiance, conditions that ensure radiation damage. For comparison, low dose rotation data was collected from a large cryocooled crystal at a synchrotron using the same photon energies. The SFX data show unusual cumulative intensity distributions, which are consistent with diffraction from a non-homogeneous distribution of crystals containing molecules displaying different degrees of local damage. Surprisingly, the electron density corresponding to the sulphur atoms of the [4Fe4S] clusters appear to be displaced from their positions as deduced from synchrotron data, indicative of correlated displacements of the atoms occurring during the accumulation time of the Bragg signals. These observations differ from the expected mere "bleaching" of the iron atoms and are suggestive of an influence of the molecular bonding and geometry on the atomic displacement dynamics following initial photoionization. The experiments are complemented by plasma code calculations.

1. Introduction

Radiation damage is one of the primary limiting factors in obtaining structural information from small and/or radiation sensitive crystals. Ultimately, it limits the maximal resolution of the data (Holton & Frankel, 2010) and can complicate the interpretation of the electron density of redox sensitive cofactors (Kuhnel *et al.*, 2007, Yano *et al.*, 2005). Recent developments at 3rd generation synchrotrons, such as better focusing optics and the use of pink beams resulting in higher flux densities, as well as faster detectors have enabled rapid data collection from micron-sized crystals, but have not solved the intrinsic problem of radiation damage (Owen *et al.*, 2014). Although cryocooling techniques slow the effects of radiation damage, the dose limit of 30 MGy (Owen *et al.*, 2006) can be reached quickly, particularly for small crystals. At room temperature, the dose limit is even lower (0.2 MGy), due to the faster diffusion of radicals, and damage becomes dose-rate dependent (Owen *et al.*, 2012). Importantly, photoreduction of metal centres already occurs at significantly lower doses,

2

complicating if not preventing the collection of chemically meaningful diffraction data using synchrotron sources (Yano *et al.*, 2005).

The femtosecond-duration X-ray pulses produced by X-ray free-electron lasers (FELs) present a novel approach to structure determination by allowing the "diffraction-before-destruction" approach in which a diffraction pattern is obtained in the short timeframe before the inevitable disintegration of the sample has progressed too far. This provides a way to circumvent the problem of radiation damage, by outrunning the slower processes contributing to the total radiation damage (Neutze *et al.*, 2000, Chapman *et al.*, 2011, Chapman *et al.*, 2014). The approach seems to work for "moderate" doses of 30-150 MGy/crystal (Boutet *et al.*, 2012, Kern *et al.*, 2013, Liu *et al.*, 2013), however, clear signs of global radiation damage are observed in the case of higher doses and longer pulses (Lomb *et al.*, 2011, Barty *et al.*, 2012). In fact, our previous experiments at the Linac Coherent Light Source (LCLS) at SLAC National Accelerator Laboratory using soft X-rays showed both a dose- and a dose rate-dependent resolution deterioration of the diffraction data of lysozyme nanocrystals for doses around 3-6 GGy (Lomb *et al.*, 2011). Both the lysozyme study and experiments using photosystem I (Barty *et al.*, 2012) showed a decrease of the high resolution diffraction signal with increasing pulse lengths. At these high dose rates, the sample is rapidly ionized. The Coulomb repulsion of the ions and the rapid rise in electron temperature lead to displacements of atoms and ions and this thermal disorder results in loss of crystalline order during the pulse, which ultimately terminates diffraction (Lomb *et al.*, 2011, Barty *et al.*, 2012).

In a first approximation to describing the processes underlying ultrafast damage, Barty *et al.* (Barty *et al.*, 2012) assumed a homogeneous distribution of atoms/elements in the unit cell, and therefore a homogeneous degree of damage. The study concluded that the FEL-induced disorder gates the diffraction, with undamaged high-resolution intensities collected at the beginning of the pulse which are superimposed with increasingly damaged, lower resolution intensities collected towards the end of the pulse. This effect was dubbed "Bragg termination" and could be correctable by a scaling algorithm.

However, homogeneous atomic disordering of the crystal lattice does not address the possibility of localised electronic damage during the femtosecond duration X-ray pulse. Simulations predict that rapid ionisation during the course of a femtosecond-duration X-ray pulse not only has the capacity to produce local changes in electron density by ionising different elements at different rates, but may also lead to modification of the atomic scattering factors themselves (Hau-Riege, 2007, Son, Young, *et al.*, 2011). This is particularly important since macromolecules and their crystals have distinctly anisotropic distributions of elements, such as oxygen-rich solvent channels, SS-bridges, metal cofactors etc. which would lead to different degrees of damage at different locations. Indeed, based on the scaling behaviour of integrated powder patterns of lysozyme nanocrystals collected with different pulse lengths, (Lomb *et al.*, 2011) predicted the existence of local damage hot spots. Such

3

inhomogeneous damage would change the molecular transform during the FEL pulse, compromising the data in a manner that cannot be rectified.

Obviously, a detailed understanding of the nature and extent of radiation damage is of tremendous importance, not only for the emerging method of serial femtosecond crystallography (SFX) but also for the development of single-particle imaging techniques using XFELs. The question of whether electronic damage is visible in electron density maps derived from high-dose FEL data is an open and pressing question of direct relevance to the study of very small and/or weakly diffracting particles or crystals that require the use of very high flux densities and doses in the high GGy range (Chapman *et al.*, 2014).

Radiation damage is initiated by inner-shell photoabsorption. Absorption cross sections are larger than scattering cross sections for most atomic species, meaning that for every scattered photon that contributes to the diffraction pattern, many more photons are absorbed and deposit their energy in the sample. At the wavelengths used in X-ray diffraction experiments, K-shell absorption dominates for low Z elements like C and S. The same holds for Fe above its K-shell absorption-edge at 7.1 keV. Below this absorption edge, the photoionization cross sections of Fe and S are similar (4,470 barns and 6,920 barns, respectively, and about 40 times higher than for C at 37 barns). The photoionization cross section of Fe increases dramatically above the K-shell absorption edge (38,000 barns), where Fe absorbs six times more above the Fe edge than S (and 340 times more than C) and therefore could be significantly more highly ionized through photoionization. Multiple ionization of iron in the high intensity FEL regime affects X-ray absorption and anomalous scattering parameters, and was proposed as a new route to phasing (Son, Chapman*, et al.*, 2011). As a first approximation, the assumption was made that only the heavy Fe atom undergoes ionization dynamics during the X-ray pulse; neither the ionization dynamics of the low Z atoms, atomic recombination associated with the large free-electron density, nor structural rearrangements (Erk *et al.*, 2013) including those causing Bragg termination (Barty *et al.*, 2012) were considered, which may affect the phasing algorithm and reconstruction. These are important issues to explore. To minimise effects of radiation damage on measured diffraction data, a detailed understanding of the influence of FEL pulse parameters such as pulse fluence and duration will enable the optimisation of experiments and the FEL sources themselves.

Here, we investigate the question of X-ray damage using the iron containing protein ferredoxin as a model system. *Clostridium acidurici* ferredoxin is a small protein (55 amino acids), containing two iron sulphur [4Fe-4S] clusters which are separated by ~12 Å, and which each have a cubane-like structure with a well-defined spatial arrangement of iron- and sulphur atoms (see Fig. 1). The structure of ferredoxin has been determined previously to 1.8 Å resolution from crystals kept at room temperature during data collection with a rotating anode (Duee *et al.*, 1994) (Tranqui & Jesior, 1995) and to 0.94 Å resolution using cryocooled crystals and synchrotron radiation, accurately defining the

geometry of the iron-sulphur centres (Dauter *et al.*, 1997). In the current study, these serve as extremely sensitive markers of ionization and thermalisation effects caused by FEL-induced radiation damage which we probed by SFX both below and above the iron K-edge. We deliberately chose to use highly damage-inducing conditions for the measurements, and to this end we used the highest available pulse energy (~1.5 mJ) and relatively long pulse duration (80 fs).

2. Material and Methods

2.1. Protein purification and crystallization

C. acidurici was obtained from the DSMZ (Deutsche Sammlung von Mikroorganismen und Zellkulturen GmbH) using the order number DSM 604 (ATCC 7906). The cells were cultured under microaerobic conditions at 30° C using DSMZ medium #76. Ferredoxin was purified essentially as described previously (Hong & Rabinowitz, 1970). For the LCLS experiments microcrystals were grown by batch crystallization mixing 100 µl protein (12 mg/ml in 15 mM Tris HCl pH 7.5, 100 mM NaCl) and 500 µl 4 M ammonium sulphate in 25 mM Tris HCl pH 7.8, 12 mM Na MOPS pH 5.8. This resulted in a rapid growth of relatively large crystals of inhomogeneous size distribution ($1.6 \pm 0.5 \times 1.6 \pm 0.5 \times 17 \pm 7.5 \ \mu m^3$) as shown in Supplemental Fig. S1. While significantly smaller crystals of very homogeneous size distribution were obtained using a protein concentration around 3 mg/ml, these crystals did not diffract to high resolution. The same protein batch used to grow the crystals for FEL data collection was used to grow macroscopic crystals for synchrotron measurements. The crystals were obtained in Linbro plates using the vapour diffusion method in the hanging drop geometry. Equal volumes of protein (6 mg/ml in 15 mM Tris HCl pH 7.5, 100 mM NaCl) and precipitant solution (3 M ammonium sulphate in 0.05 M MES pH 6.5) were mixed and equilibrated against the precipitant solution. Rod-shaped crystals appeared overnight and grew for a few days. For cryoprotection, a macroscopic ferredoxin crystal ($\sim 15 \times 15 \times 100 \ \mu m^3$) was quickly moved through a solution containing 0.1 M MES pH 7.0, 3.2 M ammonium sulphate, 10% glycerol using a standard nylon loop before flash cooling in liquid nitrogen. Macroscopic crystals were stored in liquid nitrogen until data collection.

2.2. Sample injection, post-sample attenuator characterization and data collection

FEL measurements were performed in June 2013 in the nanofocus chamber of the Coherent X-ray Imaging (CXI) instrument at the LCLS (Boutet & Williams, 2010). A suspension of ferredoxin microcrystals was injected into the FEL interaction region using a liquid microjet from a gas dynamic virtual nozzle (GDVN) (DePonte *et al.*, 2008, Weierstall *et al.*, 2012) at a flow rate of 25-30 µl/min. The LCLS provides pulses at 120 Hz, which were focused to approximately $200 \times 200 \ nm^2$ using a pair of Kirkpatrick-Baez mirrors. The X-ray pulse duration was estimated to be 80 fs from the measured

duration of the electron beam (Behrens *et al.*, 2014). The photon energy and pulse energy was 7.36 keV and 1.4 mJ and 6.86 keV and 1.6 mJ for measurements above and below the iron K edge (7.11 keV), respectively. Taking into account a beamline transmission of ~35-40 %, the power density in the focus was estimated to be on the order of 1.8×10^{19} W/cm^2.

Diffraction patterns were recorded on the CSPAD detector, version 1.2 (Philipp *et al.*, 2010). The nominal detector distance was 90 mm. To avoid saturation of and damage to the CSPAD detector, a graded W/Ta filter was placed 22 mm downstream of the interaction region, *i.e.* between the liquid jet delivering the microcrystals and the CSPAD detector. At this distance from the interaction region the transmission coefficient of the filter varied linearly from 6% at the lowest scattering angle to 15% at the highest (see Supplemental Fig. S2).

The filter (48 mm in diameter) had a 1.5 mm hole in the middle and consisted of 50 μm thick Kapton (purchased from Luxel) covered with a laterally graded $W_{0.84}Ta_{0.16}$ coating with an estimated density of 16 g/cm^3 applied by magnetron sputtering. The filter transmission was measured at different positions in the photon energy range from 4 keV to 10.5 keV at the four-crystal monochromator beamline of the Physikalisch-Technische Bundesanstalt at BESSY II where highly monochromatic radiation is available (Krumrey & Ulm, 2001). At 6.0 keV and 6.8 keV, the transmittance was mapped on a filter area of 24 mm × 48 mm with a step size of 0.4 mm and showed perfect radial symmetry (see Supplemental Fig. S2).

We collected synchrotron ferredoxin data sets at the PXIII beamline of the Swiss Light Source (SLS) using a Pilatus 2M detector. The crystal was kept at 100K during data collection. The X-ray beam was focused to 90 × 50 μm^2. The flux was 2×10^{10} photons/s and 1×10^{10} photons/s for the data sets collected using the same photon energy as for the FEL measurements above (7.36 keV) and below (6.86 keV) the iron K-edge, respectively.

2.3. Data processing, refinement and electron density map calculation

LCLS data in XTC format was processed using CASS (Foucar *et al.*, 2012). Snapshots containing more than 10 Bragg reflections were classified as hits and saved to individual HDF5 files, together with the data describing each individual FEL pulse (pulse energy, wavelength, current detector distance, etc.) corresponding to each exposure. Bragg peaks were defined as containing more than two connected pixels with at least 400 counts and identified with the post-processor no. 208 implemented in CASS. HDF5 files were analysed using CrystFEL 0.5.3a (White *et al.*, 2012). Diffraction patterns were indexed and individual intensities were then merged using Monte Carlo integration (Kirian *et al.*, 2011) using CrystFEL while excluding reflections that contained pixels with more than 3500 counts. The position as well as the roll, pitch and yaw parameters of each of the detector tiles on the multi-tile CSPAD detector were refined by minimizing the distance between indexed observed and theoretically predicted Bragg peak positions using a custom-written program, which will be described

elsewhere. This procedure increased the indexing rate of the snapshots and improved the data quality as judged by R_{split} (White *et al.*, 2012). The merged intensities from CrystFEL were converted to structure factors and saved to CCP4 (mtz) format using XDSCONV. The synchrotron data were processed with XDS (Kabsch, 1988).

Both the LCLS and SLS data were phased by molecular replacement with Phaser-MR (McCoy *et al.*, 2007) using the high-resolution ferredoxin coordinates from the Protein Data Bank (2FDN) (Dauter *et al.*, 1997) as a search model. After removing the [4Fe-4S] clusters from the model obtained with molecular replacement, 10 cycles of restrained refinement were performed using Refmac5 (Murshudov *et al.*, 2011). $2m F_{obs} - DF_{calc}$ and $mF_o - DF_c$ (Read, 1986) electron density maps were calculated, yielding unbiased omit maps of the clusters. Anomalous difference Fourier maps were calculated with the FFT program (CCP4, 1994) using phases obtained from molecular replacement. After scaling the datasets (see Supplement Table S1-5) with XSCALE (Kabsch, 1988) difference electron density maps for SLS and LCLS data (F_{obs}(SLS/LCLS)-F_{obs}(SLS/LCLS)) were calculated with the FFT program, using molecular replacement phases (Fig. S10). Electron density maps were visualized with Pymol (DeLano, 2002).

2.4. Plasma code calculations

To study the ultrafast damage dynamics in the experiment we have modelled the photon-protein interactions. To this end, we have employed the non-local thermodynamic equilibrium (non-LTE) plasma approach as implemented in the software package CRETIN (Scott, 2001). Our model does not contain detailed structural information, such as atomic positions, however it follows the atomic populations in time and includes ionization rates, electron collisions and radiation transfer. The rates from these processes are calculated, and a self-consistent rate-equation is solved, describing the evolution of the ionization and collision rates, that ultimately lead to structural degradation. This model has been used in (Barty *et al.*, 2012) to describe the global atomic disorder. For further details we refer to the simulations described in (Jönsson *et al.*, 2014) in this issue. For simplicity, we here use a flat-top X-ray pulse model. This approach keeps track of the average temperatures (we use a two temperature approach, for electrons and ions) and average ionization but excludes any local structural information, assuming that the atomic population is homogenous throughout the sample during the exposure. The sample is simulated in nanometer-sized zones, with an average atomic composition corresponding to crystalline ferredoxin ($C_{228} H_{359} N_{61} O_{83} Fe_8 S_{16}$) with water as the buffer. The density was modelled to be 1.35 g/cm^3. The simulations were done with X-ray beam parameters matching the experimental conditions, i.e. photon energies of 6.86 keV and 7.36 keV, pulse length 80 fs, pulse intensity 1.4×10^{19} W/cm^2.

3. Results and Discussion

Radiation damage at conventional X-ray sources is typically divided into two categories: global and local damage; the latter is also called specific damage. With the accumulation of the absorbed dose during data acquisition, global damage manifests itself as an overall change of the diffracted signal, such as a loss of high-resolution diffraction, an increase of the Wilson B-factor and mosaicity, as well as changes of the unit cell parameters. In contrast, local damage, such as the breakage of disulphide bonds, decarboxylation of aspartate and glutamate residues (Ravelli & McSweeney, 2000, Burmeister, 2000), or changes in oxidation and coordination states of metal cofactors (Kuhnel *et al.*, 2007, Schlichting *et al.*, 2000) results in local changes in the molecule, producing changes in individual Bragg peak intensities that cannot be accounted for by an overall scaling factor. While there is a rich history of studying radiation damage at both cryogenic and ambient temperatures using synchrotron radiation (*e.g.* (Burmeister, 2000, Ravelli *et al.*, 2003, Ravelli & McSweeney, 2000, Owen *et al.*, 2006, Kuhnel *et al.*, 2007, Owen *et al.*, 2012), few experiments have been performed so far at FEL sources. The very bright femtosecond pulses allow outrunning most damage processes, in particular those involving radical chemistry, which depend on radicals diffusing through the crystal. This has enabled the structure determination of *e.g.* the fully oxidized resting state of bovine cytochrome c oxidase, demonstrating a peroxide ligand (Hirata *et al.*, 2014) at the SACLA FEL. This study used exposure conditions that resulted in a dose of 9.9 MGy/crystal. A theoretical dose limit of 400 MGy/crystal has been proposed for FEL radiation by Chapman and coworkers (Chapman *et al.*, 2014), which, for an average protein crystal, corresponds to a dose where each atom is ionized once at the end of the pulse. Indeed, a decrease of high-resolution diffraction with increasing FEL pulse length (nominal electron bunch length 70-400 fs) was observed for doses in the GGy range, which was both dose and dose-rate dependent (Barty *et al.*, 2012, Lomb *et al.*, 2011). In particular, an increase in atomic disorder during the pulse causes thermal disordering of the crystalline lattice, resulting in a resolution-dependent termination of crystalline diffraction during the course of the X-ray pulse.

Bragg termination is reminiscent of the global damage observed at synchrotron sources, despite very different time scales and mechanisms of the radiation damage processes at the two X-ray sources. Importantly, radiation damage at synchrotrons typically accumulates over several exposures, allowing correction by zero-dose extrapolation (Diederichs, 2006). In the diffraction-before-destruction regime at FELs, however, the sample may be completely destroyed before the pulse is even over, with the decaying diffraction being integrated over the pulse duration. Measurements and simulations at different pulse irradiances may offer a way to correct for the effect of Bragg termination (Barty *et al.*, 2012).

The question of local damage in the high-intensity FEL regime remains. Based on the scaling behaviour of integrated powder patterns of lysozyme nanocrystals exposed to FEL X-ray pulses with

different pulse lengths, we had also predicted the existence of the equivalent of local damage in FEL data (Lomb *et al.*, 2011). However, the photon energy and thus the resolution of the data available at the time did not permit a study of the underlying structural changes.

Here, we set out to explore the nature of radiation damage in the high intensity regime at FEL sources, using ferredoxin as a model system. Ferredoxin contains two electron rich [4Fe-4S] clusters of intricate geometry. The behaviour of high-Z centres is of great interest due to the importance of metal centres in enzymatic catalysis, and the use of heavy metals as anomalous scatterers for phasing, in particular considering the recent proposal to use the high intensity induced electronic "bleaching" of heavier elements such as iron for new *de-novo* phasing approaches (Son, Chapman*, et al.*, 2011).

We collected SFX data of ferredoxin microcrystals using 80 fs duration X-ray pulses above and below the iron K-edge at an irradiance in the low 10^{19} W/cm^2 range. These conditions ensure significant damage and result in an average dose of ~30 GGy and ~20 GGy for each crystal above and below the Fe absorption K-edge, respectively as calculated using the RADDOSE-3D program (Zeldin *et al.*, 2013). Due to beam time limitations we were unable to explore the pulse length and fluence dependence of damage.

3.1. Overall data quality

Careful evaluation of data quality is very important in radiation damage studies to ensure that the differences observed are indeed due to damage and not to differences in experimental protocols or data quality. The former includes measurements performed at different temperatures and/or using significantly different techniques such as conventional synchrotron measurements and SFX measurements.

We collected two SFX datasets of ferredoxin microcrystals. At 7.36 keV photon energy 1,139,172 diffraction patterns were collected (in 156 minutes), 29,586 (2.6 %) of which were classified as crystal hit of which 21,706 (73.4 %) could be indexed with CrystFEL, yielding a 2.0 Å resolution dataset. At 6.86 keV photon energy 1,503,362 diffraction patterns were collected (in 210 minutes), 11,897 (0.8 %) of which were classified as crystal hits, of which 9,336 (78.5 %) could be indexed with CrystFEL, yielding a 2.1 Å resolution dataset. As the transmittance of the post-crystal attenuator varied linearly from 6 % at the lowest scattering angle to 15 % at the highest scattering angle for the photon energy of 7.36 keV, a linearly varying factor was applied to the merged intensities correcting for the transmission gradient. The factor varied linearly from 1 at the lowest resolution to 0.4 at the highest resolution. Changing the value of the correction factor at the highest resolution by ± 20 % or not applying it at all had no influence on any of the observations described below, as expected. The statistics of the two datasets are given in Table 1.

We collected low dose reference datasets at the SLS using the same photon energies from a much larger, cryocooled crystal grown from the same protein batch with very similar crystallization conditions. The crystal has the same space group and unit cell constants as the microcrystals used at the LCLS (Table 1). In the SLS case, the dose was 500 kGy and 230 kGy for the 2.0 Å and 2.1 Å resolution data sets collected above (7.36 keV) and below (6.86 keV) the Fe K-edge, respectively. The statistics of the two synchrotron (SLS) datasets is also given in Table 1.

In SFX, each crystal is hit by the FEL beam only fleetingly and does not move during the femtosecond exposure which destroys it. Thus still images are collected, containing only partial reflections. Fully integrated intensities can be obtained by Monte Carlo integration (Kirian *et al.*, 2010, Kirian *et al.*, 2011), which merges all measured partial intensities, averaging out all fluctuations occurring during data collection (different crystal sizes, incident beam intensities, spectral fluctuations of the FEL beam etc.), provided enough individual measurements exist for each unique reflection. This dependence explains the poorer data statistics of the 6.86 keV LCLS data set compared to that of the 7.36 keV LCLS data set, as it contains only half the number of indexed patterns. Indeed, the difference in signal to noise ratio and R_{split} between the two data sets corresponds approximately to the factor of $\sqrt{2}$ expected for a two-fold difference in the number of observations. However, the average multiplicity of the 6.86 keV SFX data is ~170, which is in the same range as for other high resolution SFX structures (e.g. (Boutet *et al.*, 2012)). Despite having similar multiplicities, resolution (2.1 Å in this study and 1.9 Å in Boutet *et al.*) and the same space group ($P4_32_12$), the data statistics are not as good, in particular when considering R_{split} (see Table 1). The relatively poor statistics of the ferredoxin data is even more significant when taking into account that the Boutet *et al.* lysozyme data were collected using an earlier version of the CSPAD detector and were processed using a cruder detector geometry correction. The poor statistics are unlikely to be due to non-isomorphism of the microcrystals, since the unit cell distribution is relatively narrow (see Supplemental Fig. S3), and agrees with the one observed in macroscopic ferredoxin crystals. Data of these crystals are highly isomorphous (data not shown).

We scaled the LCLS and SLS data using XSCALE (Kabsch, 1988) (see Supplement Table S1-5). For the 7.36 keV (6.86 keV) data the correlation coefficient was 0.74 (0.76) for 2561 (2333) common reflections. The correlation of the LCLS data with the SLS data is low and similar to the correlation between the deposited room temperature and cryocooled data from pdb entries 1fdn and 2fdn, respectively. Incidentally, the correlations are on the order of those expected for a heavy atom derivative, and it is thus conceivable that the low correlations at least in part also reflect a degree of local radiation damage to the iron-sulphur clusters.

When we analysed the intensity distribution of the ferredoxin diffraction data by generating Wilson- and cumulative intensity distribution plots for the LCLS and synchrotron data sets, it became apparent that the LCLS SFX data sets differ from the expected distributions, which are exemplified by the synchrotron rotation data (see Supplemental Fig. S4). In particular, both strong and weak intensities are underrepresented in the FEL data. This effect is independent of the resolution limits used (not shown) and so is unlikely to be the result of difficulties with the integration of weak spots at the edge of the detector, a common problem in SFX.

To investigate whether the unusual intensity distribution of the FEL data could be due to local damage to the iron-sulphur clusters, which are responsible for a considerable fraction of the total scattering, we calculated structure factors (F_{calc}) for ferredoxin with and without coordinates of the two [4Fe-4S] clusters included, identifying a number of reflections that differ significantly in magnitude. We then analysed the ratio of intensities of these reflections between the synchrotron data (corresponding to the situation with full cluster) and FEL data (corresponding to the situation with a potentially damaged cluster) and compared this to ratios of randomly chosen pairs of reflections. No correlation between the calculated and observed pairs of reflections was observed (see Supplement Fig. S5). We next simulated the effect of Bragg termination on the Wilson and intensity distribution statistics by modifying the low-dose synchrotron intensities using formula 3 from Barty *et al.*, assuming average atomic displacements of either 10 Å (the maximum value expected according to (Chapman *et al.*, 2014)) or 40 Å (chosen to clarify the effect) at the end of the pulse. This, however, neither reproduced the observed Wilson plots nor the cumulative intensity distributions observed for the LCLS data (see Supplement Fig. S6). This could be explained by assuming that under the conditions of the current experiment, the ionization effects are so strong (as outlined below) that ionization will cause termination of the Bragg diffraction (Caleman *et al.*, (under review)), rather than the increasing disorder in the structure as described by Barty *et al* .

In fact, in case of the cumulative intensity distribution for the 40 Å displacement Bragg termination simulation, the curve for acentric reflections even lies above the expected distribution rather than below as observed for the LCLS ferredoxin data. However, it is noteworthy that several LCLS datasets of other proteins indeed show such an effect (data not shown), which thus could be explained by Bragg termination.

For SFX data from ferredoxin, however, the cumulative intensity distributions do not only lie below the expected curve, but are actually sigmoidal, as those expected for the cumulative intensity distribution from a twinned crystal. This is indicative of an 'averaging' of intensities, which can only be caused by a summation of different structure factor amplitudes, not by global damage effects such as an increased B-factor or Bragg termination, which do not affect the structure factors but modulate the intensities in a continuous, resolution-dependent fashion. A possible scenario explaining this could be different degrees of damage for different crystals, or different parts of the crystals being damaged

11

to a different extent. This is in line with our experimental setup, which involves crystals that are significantly larger than the intense X-ray nanofocus. Thus, only small parts of the crystals will be exposed to the focussed beam while significantly larger parts of the crystals will be grazed by the "halo" around the focussed X-ray beam. Given the strong scattering power of the crystals, even very weak parts of the X-ray beam are likely to result in appreciable diffraction signal.

To illustrate this hypothesis, we averaged structure factors calculated from five ferredoxin models, to which random shifts of the atoms of up to 1.5 Å had been applied. The resulting averaged structure factor amplitudes indeed showed the expected sigmoidal cumulative intensity distribution (see Supplement Fig. S7).

Given the unusual cumulative intensity distribution, we were interested in the information content of the SFX intensities. Therefore, we calculated simulated annealed omit maps for the 7.4 keV synchrotron and FEL data. The correlation coefficient between the two maps CC_{map} is 0.63. As can be seen in Supplemental Fig. S8, omitting the coordinates of a tyrosine residue from the model results in excellent difference electron density in the case of the synchrotron data in contrast to the situation for the SFX data, where no interpretable difference density was apparent. This shows that the information content of our SFX data is rather low. This is remarkable, given that the multiplicity of our SFX data far exceeds that of e.g. the SFX data of the *B. viridis* photosynthetic reaction centre, which was ~27, and that difference maps calculated from those data clearly showed cofactors etc. (Johansson *et al.*, 2013). This makes it very unlikely that the low information content and low data quality are due to poor convergence of the Monte-Carlo integration.

3.2. The iron sulphur clusters

C. acidiurici ferredoxin contains two iron-sulphur clusters, cluster 1 (consisting of Fe1-SG8, Fe2-SG11, Fe3-SG14, Fe4-SG47, same nomenclature as used by (Dauter *et al.*, 1997) with SG indicating the thiol sulphur of the coordinating cysteine residue) and cluster 2 (Fe1-SG37 Fe2-SG40, Fe3-SG43, Fe4-SG18). The occupancy of the two iron sulphur clusters can vary between different protein preparations, depending on both the growth conditions of the bacterial cells as well as the details of the protein purification protocol. To avoid any influence on the data from these purely biochemical factors, we used the same protein sample to obtain the crystals used for measurements at both the LCLS and the SLS. Importantly, the SLS crystals were grown after the LCLS beamtime, eliminating protein degradation as a possible source for the observation of lower cluster occupancy in the FEL data.

In contrast to the polypeptide part of the structure, clearly defined density is observed in simulated annealing composite omit maps for these iron-sulphur clusters. Moreover, as shown below, there is significant anomalous difference density (see Supplemental Fig. S9) at the iron positions of the

clusters, suggesting that the data are better than expected from the statistics described in the previous section.

Strikingly, in omit maps, there are distinct positive difference density peaks close to the sulphurs but on the outside of the clusters (Fig.1). In particular, sulphur atoms S1, S2, S4 of cluster 1 and sulphur atoms S1, S3 of cluster 2 are not at the expected atom locations but have moved away from the centre of the clusters. This effect is strong enough to come out of any model bias after simulated annealing, as it is also visible when the clusters are part of the model.

This observation implies a correlated movement of the atoms, in line with a partial expansion or distortion of the clusters (see Fig. 1). This effect is not due to the fact that the LCLS data were collected at room temperature, as a comparison of the 2FDN synchrotron structure with an earlier structure (1FDN, (Duee *et al.*, 1994)) determined at room temperature shows that the iron-sulphur clusters have the same structure at both temperatures.

Photoabsorption depends strongly on the atomic number, rendering metal centres such as the iron sulphur clusters in ferredoxin highly susceptible to radiation damage. Since the crystals used for the FEL and synchrotron measurements are largely isomorphous, it is possible to calculate difference electron density maps (F_{obs} (SLS) – F_{obs} (LCLS)). However, the effects of the loss of electrons through ionization, increased temperature factors due to disorder, correlated motion of cluster atoms (such as *e.g.* an expansion) as well as effects caused by different experimental protocols such as different data collection temperatures would all manifest themselves as difference peaks and it would be very difficult to disentangle the various causes. We therefore abandoned this analysis.

In order to get unbiased electron densities of the [4Fe-4S] clusters we performed 10 cycles of restrained refinement in Refmac5 (Murshudov *et al.*, 2011) with the clusters omitted from the 2FDN model (Dauter *et al.*, 1997) used as the starting model for refinement, before calculating $2mF_{obs}$ - DF_{calc} and mF_o - DF_c maps (Read, 1986) for the two ferredoxin data sets collected at LCLS and SLS, above and below the iron K-shell absorption edge, respectively. The results are shown in Fig. 1 (LCLS data) and Fig. 2 (SLS data) with the cluster coordinates superimposed as a reference for the positions of Fe and S atoms in the undamaged clusters.

SFX has been shown to give accurate structures in good agreement with synchrotron structures (Boutet *et al.*, 2012, Liu *et al.*, 2013), *e.g.* we have shown that at doses of ~3 and 33 MGy, and using pulse lengths of 5 and 40 fs, SFX data from lysozyme agree well with low-dose synchrotron datasets (Boutet *et al.*, 2012).

Given the difference in the photoionization cross section ratios of Fe and S above ($\sigma_{Fe}/\sigma_S = 5.6$) and below ($\sigma_{Fe}/\sigma_S = 0.7$) the Fe K-edge, we expected significantly higher ionization of iron in the 7.4 keV dataset. However, neither the difference electron density map calculated between the SLS

($F_{obs}(SLS_{7.4keV})$ - $F_{obs}(SLS_{6.9keV})$)) nor the LCLS ($F_{obs}(LCLS_{7.4keV})$ - $F_{obs}(LCLS_{6.9keV})$)) data above and below the iron K absorption edge show strong features at the iron positions (see Supplement Fig. S10). Interestingly, in the LCLS difference map there are positive electron density peaks at the sulphur positions of cysteine residues 8, 14, 18, 37, and 43 which keep the clusters in place in the structure.

3.3. Ultrafast damage processes

Radiation damage processes in proteins are strongly modified by the presence of atoms with high atomic numbers (Z) , rendering metal centres such as the iron sulphur clusters in Ferredoxin particularly susceptible to ionisation, since such atoms will lose proportionally more electrons by direct photoionisation than will lighter atoms. Damage is initiated by inner-shell photoabsorption. The excited atoms quickly relax through non-radiative Auger decay, which is more probable than radiative decay even for Fe. Auger decay occurs much more rapidly in Fe (0.55 fs) and S (1.3 fs) than in C (10 fs) (see (Chapman *et al.*, 2014)), and can be considered to be instantaneous for the 80 fs pulse length used in this study. With typical velocities between 60 and 500 Å/fs, the Auger and photoelectrons generate electron cascades through electron impact ionization, leading to the emission of secondary electrons with velocities below 30 Å/fs. It has been estimated that one 6 keV photoelectron will lead to 300 secondary electrons, and each Auger electron will give 10-20 secondary electrons (Caleman, Huldt*, et al.*, 2011). All cascades are within 10 fs from the initial photoionization event, thus well within the pulse length (Caleman, Bergh*, et al.*, 2011, Chapman *et al.*, 2014). On a large scale, the electrons quickly equilibrate among themselves and will couple with the ions though collisions, leading to a hydrodynamic expansion of the molecule. In addition, the ions are expected to reconfigure on a local scale, which depends on the local atomic arrangement. Inhomogeneous distributions of atomic elements in molecules, in particular the presence of strongly absorbing Fe, is expected to significantly alter the local damage response.

We clearly observe both global and local effects of radiation damage in the ferredoxin SFX data as expected given the experimental conditions of very high flux density, long FEL pulse length and the associated high dose absorbed by each microcrystal. Using plasma simulations (Scott, 2001, Caleman, Bergh*, et al.*, 2011) we can explore the underlying effects of ionization and displacement of the atoms, electrons and ions, respectively, and the influence on the global damage. Fig. 3a shows the average ionization for C, S and Fe as a function of time during the pulse, for photon energies below and above the Fe K-edge. The simulations show that all atoms rapidly lose electrons at the beginning of the exposure, reaching a high ionization state by the end of the 80 fs pulse. Furthermore, the ionization states for Fe above and below the edge is quite similar and suggests that it is more influenced by collisional ionization than direct photoionization. To estimate how the rapid change in ionization will change the diffracted signal, we estimate the scattering to be proportional to the

squared number of electrons left in the atoms. Figure 3 shows the instantaneous scattering power of each atomic species (C,S,Fe) as a function of time (Fig. 3b) and also the integrated signal as it accumulates during the pulse (Fig. 3c). The results suggest that most of the diffracted signal comes from the first 10-30 fs depending on the element, while the choice of wavelength only affects the contribution from the Fe.

Barty *et al.* describes the decay of the Bragg signal as a function of atomic displacement, using a disorder factor. In that study the root mean square displacement followed a $t^{3/2}$ time-dependence. The decay of the Bragg signal due to ionization was omitted in that model. Based on our simulations (Fig. 3) we expect the ionization to play an important role in the present study, and we would expect that the description presented in Barty *et al.* should not reproduce our data as is indeed the case (Supplement Fig. S6). We have earlier calculated atomic displacements for light atoms (Barty *et al.*, Chapman *et al.*, 2014) based on a model of ion diffusion in homogeneous solid density plasma. (Chapman *et al.*, 2014) shows the calculated root mean square deviation (RMSD) of the C atoms as a function of dose. In our model, RMSD scales with $1/\sqrt{m}$ and we expect the displacement for Fe to be a factor 2 lower than for C. We also find that RMSD scales roughly with time as $t^{3/2}$ during the pulse, which implies that Fe ions will reach the same disorder as C delayed by a factor 1.5 in time. With this scaling, if C atoms reach 1Å disorder in 20 fs for a dose of about 400 MGy/fs (Chapman *et al.*, 2014), then Fe ions would reach the same 1Å disorder in 30 fs. Taking into account both ionization dynamics and displacement, our simulations show that only the first 20-30 fs in the exposure are relevant for the resolution we are looking at, and that the diffracted signal could be quite sensitive to which of the ionization or disorder dynamics happen first.

It is unexpected to observe distinct electron density peaks for some of the sulphur atoms of the clusters at positions that differ from those of an undamaged cluster (Fig. 1). This effect, which is much stronger for cluster 1 than cluster 2, would imply a correlated movement by 0.3 – 0.5 Å of these sulphur atoms in a significant number of all ferredoxin molecules in all crystals that were used for the complete data set. This could be due to a repulsion of the sulphur atoms from the more rapidly ionizing heavier iron atoms (Jurek & Faigel, 2009). The observation of distinct electron density peaks in cluster 1 would be consistent with a stable intermediate likely forming within the first 20 fs during the X-ray pulse duration (see above) before the onset of significant disorder. The densities in cluster 2 are more elongated, expanding from the expected position which would be in line with scattering contributions of the undamaged molecule at the beginning of the pulse superimposed with increasingly displaced conformations during the pulse duration. This displacement effect was only observed for the "free" sulphurs of the cluster, but not the thiolate sulphurs of the coordinating cysteine residues. Interestingly, most of these latter sulphurs show electron density in the LCLS ($F_{obs}(LCLS_{7.4keV})$ - $F_{obs}(LCLS_{6.9keV})$) difference maps.

We speculate that the basis for all these observations might be an ultrafast charge rearrangement between the ionized iron and the coordinating sulphur. Such an effect has been observed recently in methylselenol molecules exposed to intense ($> 10^{17}$ W/cm^2) ultra-short 2 keV FEL pulses. An ultrafast charge redistribution from the inner-shell ionized selenium to the other atoms in the molecule takes place as well as significant displacement of the atomic constituents upon multiple ionization during the pulse (Erk *et al.*, 2013). The effect of FEL pulses on biological samples containing heavy atoms or non-homogeneous spatial distributions of atoms have been analysed by (Jurek & Faigel, 2009) using molecular-dynamics-type modelling. Significantly increased local distortions were predicted in the vicinity of heavy atoms as well as changes in the time evolution of the atomic displacements. We therefore speculate that a charge migration between irons and sulphurs takes place in the clusters, followed by both correlated and slower uncorrelated displacements.

4. Conclusions

It is well known in conventional crystallography that the sites of high-Z atoms are prone to higher levels of radiation damage. Our results here suggest that a similar situation is encountered in the high-intensity FEL regime. Although the details of the damage mechanisms differ between FEL and synchrotron sources, our results suggest that even small differences in coordination and environment may affect the extent of radiation damage in the high intensity regime at FELs. While we realize that the conditions chosen for our experiment are unlikely to be those chosen for realistic data collection schemes (given the very long pulse lengths) the results nevertheless demonstrate that FEL-induced radiation damage is far from being understood.

We cannot completely exclude the possibility that our results are at least in part compromised by non-damage related differences between the FEL data and the synchrotron data used as a reference. First, there is the difference in collection temperature (room temperature for the LCLS data vs. cryogenic data collection at the SLS). However, as mentioned before, this cannot explain the apparent displacement of the sulphur atoms in the clusters since in a conventionally determined room-temperature structure, the clusters have the same structure as at 100 K. Second, microcrystals were used for the LCLS data whereas the SLS data were collected from a single macroscopic crystal. However, the unit cell parameters of the LCLS data are very similar to those of the SLS data, making it very unlikely that the observed effects are due to nonisomorphism. Third, there is the fact that different methods were used (serial crystallography vs. rotation data collection) and that there are differences in the data quality. However, differences in global data quality would necessarily affect the entire electron density map, and never lead to features at specific locations such as the iron-sulfur clusters, as these are not on symmetry axes or other special positions. Moreover, the low-resolution completeness of the LCLS data is 100% with an average redundancy ~460 (see Table S6f), making it

unlikely that the absence of low-resolution reflections causes e.g. the differences observed between the clusters.

Thus, while caution is appropriate, this study provides a first, tantalising glimpse of local damage processes on femtosecond timescales in the extremely high intensity regime. More experiments, systematically probing the FEL pulse length and fluence and thus dose and dose rate are therefore needed, as well as detailed calculations and new theoretical tools exploring the effects described here.

Acknowledgements

References

Barends, T. R., Foucar, L., Shoeman, R. L., Bari, S., Epp, S. W., Hartmann, R., Hauser, G., Huth, M., Kieser, C., Lomb, L., Motomura, K., Nagaya, K., Schmidt, C., Strecker, R., Anielski, D., Boll, R., Erk, B., Fukuzawa, H., Hartmann, E., Hatsui, T., Holl, P., Inubushi, Y., Ishikawa, T., Kassemeyer, S., Kaiser, C., Koeck, F., Kunishima, N., Kurka, M., Rolles, D., Rudek, B., Rudenko, A., Sato, T., Schroeter, C. D., Soltau, H., Strueder, L., Tanaka, T., Togashi, T., Tono, K., Ullrich, J., Yase, S., Wada, S. I., Yao, M., Yabashi, M., Ueda, K. & Schlichting, I. (2013). *Acta Crystallogr.D.Biol.Crystallogr.* **69**, 838-842.
Barty, A., Caleman, C., Aquila, A., Timneanu, N., Lomb, L., White, T. A., Andreasson, J., Arnlund, D., Bajt, S., Barends, T. R., Barthelmess, M., Bogan, M. J., Bostedt, C., Bozek, J. D., Coffee, R., Coppola, N., Davidsson, J., DePonte, D. P., Doak, R. B., Ekeberg, T., Elser, V., Epp, S. W., Erk, B., Fleckenstein, H., Foucar, L., Fromme, P., Graafsma, H., Gumprecht, L., Hajdu, J., Hampton, C. Y., Hartmann, R., Hartmann, A., Hauser, G., Hirsemann, H., Holl, P., Hunter, M. S., Johansson, L., Kassemeyer, S., Kimmel, N., Kirian, R. A., Liang, M., Maia, F. R., Malmerberg, E., Marchesini, S., Martin, A. V., Nass, K., Neutze, R., Reich, C., Rolles, D., Rudek, B., Rudenko, A., Scott, H., Schlichting, I., Schulz, J., Seibert, M. M., Shoeman, R. L., Sierra, R. G., Soltau, H., Spence, J. C., Stellato, F., Stern, S., Struder, L., Ullrich, J., Wang, X., Weidenspointner, G., Weierstall, U., Wunderer, C. B. & Chapman, H. N. (2012). *Nat.Photonics.* **6**, 35-40.
Behrens, C., Decker, F.-J., Ding, Y., Dolgashev, V. A., Frisch, J., Huang, Z., Krejcik, P., Loos, H., Lutman, A., Maxwell, T. J., Turner, J., Wang, J., Wang, M.-H., Welch, J. & Wu, J. (2014). *Nature Communications* **5**, 3762.
Boutet, S., Lomb, L., Williams, G. J., Barends, T. R. M., Aquila, A., Doak, R. B., Weierstall, U., Deponte, D., Steinbrener, J., Shoeman, R. L., Messerschmidt, M., Barty, A., White, T. A., Kassemeyer, S., Kirian, R. A., Seibert, M. M., Montanez, P. A., Kenney, C., Herbst, R., Hart, P., Pines, J., Haller, G., Gruner, S. M., Philipp, H. T., Tate, M. W., Hromalik, M., Koerner, L. J., van Bakel, N., Morse, J., Ghonsalves, W., Arnlund, D., Bogan, M. J., Caleman, C., Fromme, R., Hampton, C. Y., Hunter, M. S., Johansson, L., Katona, G., Kupitz, C., Liang, M., Martin, A. V., Nass, K., Redecke, L., Stellato, F., Timneanu, N., Wang, D., Zatsepin, N. A., Schafer, D., Defever, J., Neutze, R., Fromme, P., Spence, J. C. H., Chapman, H. N. & Schlichting, I. (2012). *Science* **337**, 362-364.
Boutet, S. & Williams, G. J. (2010). *New Journal of Physics* **12**.
Burmeister, W. P. (2000). *Acta Crystallogr.D Biol.Crystallogr.* **56**, 328-341.
Caleman, C., Bergh, M., Scott, H. A., Spence, J. C. H., Chapman, H. N. & Timneanu, N. (2011). *Journal of Modern Optics* **58**, 1486-1497.
Caleman, C., Huldt, G., Maia, F. R. N. C., Ortiz, C., Parak, F. G., Hajdu, J., van der Spoel, D., Chapman, H. N. & Timneanu, N. (2011). *Acs Nano* **5**, 139-146.
Caleman, C., Timneanu, N., Martin, A. V., Jönsson, H. O., Aquila, A., Barty, A., Scott, H., White, T. A. & Chapman, H. N. ((under review)).
CCP4 (1994). *Acta crystallographica. Section D, Biological crystallography* **50**, 760–763.
Chapman, H. N., Caleman, C. & Timneanu, N. (2014). *Phil.Trans.R.Soc.B* **369**, 20130313.
Chapman, H. N., Fromme, P., Barty, A., White, T. A., Kirian, R. A., Aquila, A., Hunter, M. S., Schulz, J., DePonte, D. P., Weierstall, U., Doak, R. B., Maia, F. R. N. C., Martin, A. V., Schlichting, I., Lomb, L., Coppola, N., Shoeman, R. L., Epp, S. W., Hartmann, R., Rolles, D., Rudenko, A., Foucar, L., Kimmel, N., Weidenspointner, G., Holl, P., Liang, M., Barthelmess, M., Caleman, C., Boutet, S., Bogan, M. J., Krzywinski, J., Bostedt, C., Bajt, S., Gumprecht, L., Rudek, B., Erk, B., Schmidt, C., Homke, A., Reich, C., Pietschner, D., Struder, L., Hauser, G., Gorke, H., Ullrich, J., Herrmann, S., Schaller, G., Schopper, F., Soltau, H., Kuhnel, K. U., Messerschmidt, M., Bozek, J. D., Hau-Riege, S. P., Frank, M., Hampton, C. Y., Sierra, R. G., Starodub, D., Williams, G. J., Hajdu, J., Timneanu, N., Seibert, M. M., Andreasson, J., Rocker, A., Jonsson, O., Svenda, M., Stern, S., Nass, K., Andritschke, R., Schroter, C. D., Krasniqi, F., Bott, M., Schmidt, K. E., Wang, X., Grotjohann, I., Holton, J. M., Barends, T. R. M., Neutze, R., Marchesini, S., Fromme, R., Schorb, S., Rupp, D., Adolph, M., Gorkhover, T., Andersson, I., Hirsemann, H., Potdevin, G., Graafsma, H., Nilsson, B. & Spence, J. C. H. (2011). *Nature* **470**, 73-77.
Dauter, Z., Wilson, K. S., Sieker, L. C., Meyer, J. & Moulis, J. M. (1997). *Biochemistry* **36**, 16065-16073.
DeLano, W. L. (2002). *The PyMOL Molecular Graphics System.*
DePonte, D. P., Weierstall, U., Schmidt, K., Warner, J., Starodub, D., Spence, J. C. H. & Doak, R. B. (2008). *Journal of Physics D-Applied Physics* **41**.
Diederichs, K. (2006). *Acta Crystallogr.D Biol.Crystallogr.* **62**, 96-101.
Duee, E. D., Fanchon, E., Vicat, J., Sieker, L. C., Meyer, J. & Moulis, J. M. (1994). *Journal of Molecular Biology* **243**, 683-695.
Erk, B., Rolles, D., Foucar, L., Rudek, B., Epp, S. W., Cryle, M., Bostedt, C., Schorb, S., Bozek, J., Rouzee, A., Hundertmark, A., Marchenko, T., Simon, M., Filsinger, F., Christensen, L., De, S., Trippel, S., Kupper, J., Stapelfeldt, H., Wada, S., Ueda, K., Swiggers, M., Messerschmidt, M., Schroter, C. D., Moshammer, R., Schlichting, I., Ullrich, J. & Rudenko, A. (2013). *Phys.Rev.Lett.* **110**, 053003.
Foucar, L., Barty, A., Coppola, N., Hartmann, R., Holl, P., Hoppe, U., Kassemeyer, S., Kimmel, N., Kupper, J., Scholz, M., Techert, S., White, T. A., Struder, L. & Ullrich, J. (2012). *Comput.Phys.Commun.* **183**, 2207.
Hau-Riege, S. P. (2007). *Physical Review A* **76**.
Hirata, K., Shinzawa-Itoh, K., Yano, N., Takemura, S., Kato, K., Hatanaka, M., Muramoto, K., Kawahara, T., Tsukihara, T., Yamashita, E., Tono, K., Ueno, G., Hikima, T., Murakami, H., Inubushi, Y., Yabashi, M., Ishikawa, T., Yamamoto, M., Ogura, T., Sugimoto, H., Shen, J. R., Yoshikawa, S. & Ago, H. (2014). *Nat.Methods* **11**, 734-736.
Holton, J. M. & Frankel, K. A. (2010). *Acta Crystallogr.D Biol.Crystallogr.* **66**, 393-408.
Hong, J. S. & Rabinowitz, J. C. (1970). *J Biol.Chem.* **245**, 4982-4987.
Johansson, L. C., Arnlund, D., Katona, G., White, T. A., Barty, A., DePonte, D. P., Shoeman, R. L., Wickstrand, C., Sharma, A., Williams, G. J., Aquila, A., Bogan, M. J., Caleman, C., Davidsson, J., Doak, R. B., Frank, M., Fromme, R., Galli, L., Grotjohann, I., Hunter, M. S., Kassemeyer, S., Kirian, R. A., Kupitz, C., Liang, M., Lomb, L., Malmerberg, E., Martin, A. V., Messerschmidt, M., Nass, K., Redecke, L., Seibert, M. M., Sjoehamn, J., Steinbrener, J., Stellato, F., Wang, D., Wahlgren, W. Y., Weierstall, U., Westenhoff, S., Zatsepin, N. A., Boutet, S., Spence, J. C. H., Schlichting, I., Chapman, H. N., Fromme, P. & Neutze, R. (2013). *Nature Communications* **4**.
Jönsson, O. H., Timneanu, N., Ostlin, C., Scott, H. A. & Caleman, C. (2014). *Journal of Synchrotron Radiation* **this issue**.
Jurek, Z. & Faigel, G. (2009). *EPL (Europhysics Letters)* **86**, 68003.
Kabsch, W. (1988). *Journal of Appl.Cryst.* **21**, 916-924.

Kern, J., onso-Mori, R., Tran, R., Hattne, J., Gildea, R. J., Echols, N., Glockner, C., Hellmich, J., Laksmono, H., Sierra, R. G., Lassalle-Kaiser, B., Koroidov, S., Lampe, A., Han, G., Gul, S., Difiore, D., Milathianaki, D., Fry, A. R., Miahnahri, A., Schafer, D. W., Messerschmidt, M., Seibert, M. M., Koglin, J. E., Sokaras, D., Weng, T. C., Sellberg, J., Latimer, M. J., Grosse-Kunstleve, R. W., Zwart, P. H., White, W. E., Glatzel, P., Adams, P. D., Bogan, M. J., Williams, G. J., Boutet, S., Messinger, J., Zouni, A., Sauter, N. K., Yachandra, V. K., Bergmann, U. & Yano, J. (2013). *Science* **340**, 491-495.

Kirian, R. A., Wang, X., Weierstall, U., Schmidt, K. E., Spence, J. C. H., Hunter, M., Fromme, P., White, T., Chapman, H. N. & Holton, J. (2010). *Optics Express* **18**, 5713-5723.

Kirian, R. A., White, T. A., Holton, J. M., Chapman, H. N., Fromme, P., Barty, A., Lomb, L., Aquila, A., Maia, F. R., Martin, A. V., Fromme, R., Wang, X., Hunter, M. S., Schmidt, K. E. & Spence, J. C. (2011). *Acta Crystallogr.A* **67**, 131-140.

Krumrey, M. & Ulm, G. (2001). *Nuclear Instruments and Methods in Physics Research Section A: Accelerators, Spectrometers, Detectors and Associated Equipment* **467–468, Part 2**, 1175-1178.

Kuhnel, K., Derat, E., Terner, J., Shaik, S. & Schlichting, I. (2007). *Proc.Natl.Acad.Sci.U.S.A* **104**, 99-104.

Liu, W., Wacker, D., Gati, C., Han, G. W., James, D., Wang, D., Nelson, G., Weierstall, U., Katritch, V., Barty, A., Zatsepin, N. A., Li, D., Messerschmidt, M., Boutet, S., Williams, G. J., Koglin, J. E., Seibert, M. M., Wang, C., Shah, S. T., Basu, S., Fromme, R., Kupitz, C., Rendek, K. N., Grotjohann, I., Fromme, P., Kirian, R. A., Beyerlein, K. R., White, T. A., Chapman, H. N., Caffrey, M., Spence, J. C., Stevens, R. C. & Cherezov, V. (2013). *Science* **342**, 1521-1524.

Lomb, L., Barends, T. R., Kassemeyer, S., Aquila, A., Epp, S. W., Erk, B., Foucar, L., Hartmann, R., Rudek, B., Rolles, D., Rudenko, A., Shoeman, R. L., Andreasson, J., Bajt, S., Barthelmess, M., Barty, A., Bogan, M. J., Bostedt, C., Bozek, J. D., Caleman, C., Coffee, R., Coppola, N., DePonte, D. P., Doak, R. B., Ekeberg, T., Fleckenstein, H., Fromme, P., Gebhardt, M., Graafsma, H., Gumprecht, L., Hampton, C. Y., Hartmann, A., Hauser, G., Hirsemann, H., Holl, P., Holton, J. M., Hunter, M. S., Kabsch, W., Kimmel, N., Kirian, R. A., Liang, M., Maia, F. R., Meinhart, A., Marchesini, S., Martin, A. V., Nass, K., Reich, C., Schulz, J., Seibert, M. M., Sierra, R., Soltau, H., Spence, J. C., Steinbrener, J., Stellato, F., Stern, S., Timneanu, N., Wang, X., Weidenspointner, G., Weierstall, U., White, T. A., Wunderer, C., Chapman, H. N., Ullrich, J., Struder, L. & Schlichting, I. (2011). *Phys.Rev.B Condens.Matter Mater.Phys.* **82**, 214111.

McCoy, A. J., Grosse-Kunstleve, R. W., Adams, P. D., Winn, M. D., Storoni, L. C. & Read, R. J. (2007). *Journal of applied crystallography* **40**, 658-674.

Murshudov, G. N., Skubak, P., Lebedev, A. A., Pannu, N. S., Steiner, R. A., Nicholls, R. A., Winn, M. D., Long, F. & Vagin, A. A. (2011). *Acta crystallographica. Section D, Biological crystallography* **D67**, 355-367.

Neutze, R., Wouts, R., van der Spoel, D., Weckert, E. & Hajdu, J. (2000). *Nature* **406**, 752-757.

Owen, R. L., Axford, D., Nettleship, J. E., Owens, R. J., Robinson, J. I., Morgan, A. W., Dore, A. S., Lebon, G., Tate, C. G., Fry, E. E., Ren, J., Stuart, D. I. & Evans, G. (2012). *Acta Crystallogr.D Biol.Crystallogr.* **68**, 810-818.

Owen, R. L., Paterson, N., Axford, D., Aishima, J., Schulze-Briese, C., Ren, J., Fry, E. E., Stuart, D. I. & Evans, G. (2014). *Acta Crystallogr.D Biol.Crystallogr.* **70**, 1248-1256.

Owen, R. L., Rudino-Pinera, E. & Garman, E. F. (2006). *Proc.Natl.Acad.Sci.U.S.A* **103**, 4912-4917.

Philipp, H. T., Koerner, L. J., Hromalik, M. S., Tate, M. W. & Gruner, S. M. (2010). *Ieee Transactions on Nuclear Science* **57**, 3795-3799.

Ravelli, R. B., Leiros, H. K., Pan, B., Caffrey, M. & McSweeney, S. (2003). *Structure.* **11**, 217-224.

Ravelli, R. B. G. & McSweeney, S. M. (2000). *Structure* **8**, 315-328.

Read, R. J. (1986). *Acta Crystallographica* **42**, 140-149.

Schlichting, I., Berendzen, J., Chu, K., Stock, A. M., Maves, S. A., Benson, D. E., Sweet, R. M., Ringe, D., Petsko, G. A. & Sligar, S. G. (2000). *Science* **287**, 1615-1622.

Scott, H. A. (2001). *Journal of Quantitative Spectroscopy & Radiative Transfer* **71**, 689-701.

Son, S.-K., Chapman, H. N. & Santra, R. (2011). *Phys.Rev.Lett.* **107**, 218102.

Son, S.-K., Young, L. & Santra, R. (2011). *Physical Review A* **83**.

Tranqui, D. & Jesior, J. C. (1995). *Acta Crystallographica Section D-Biological Crystallography* **51**, 155-159.

Weierstall, U., Spence, J. C. & Doak, R. B. (2012). *Rev.Sci.Instrum.* **83**, 035108.

White, T. A., Kirian, R. A., Martin, A. V., Aquila, A., Nass, K., Barty, A. & Chapman, H. N. (2012). *J Appl Cryst.* **45**, 335-341.

Yano, J., Kern, J., Irrgang, K. D., Latimer, M. J., Bergmann, U., Glatzel, P., Pushkar, Y., Biesiadka, J., Loll, B., Sauer, K., Messinger, J., Zouni, A. & Yachandra, V. K. (2005). *Proc.Natl.Acad.Sci.U.S.A* **102**, 12047-12052.

Zeldin, O. B., Gerstel, M. & Garman, E. F. (2013). *Journal of applied crystallography* **46**, 1225-1230.

Table 1 Data collection statistics

Data set name	LCLS 7.36 keV	LCLS 6.86 keV	SLS 7.36 keV	SLS 6.86 keV
Software	CrystFEL 0.5.3a	CrystFEL 0.5.3a	XDS	XDS
Data collection				
Wavelength ($\mathring{A}$)	1.685 ± 0.001	1.807 ± 0.001	1.685	1.807
Photon energy (keV)	7.36	6.86	7.36	6.86
Pulse energy (mJ)	1.4 ± 0.1	1.6 ± 0.1	-	-
Pulse duration (fs)*	80 ± 3	80 ± 3	-	-
Power density (W/cm^2)	1.8×10^{19}	1.7×10^{19}	-	-
Crystals				
Dimensions [μm^3]	$1.6\pm0.5\times1.6\pm0.5\times17\pm7.5$	$1.6\pm0.5\times1.6\pm0.5\times17\pm7.5$	$15\times15\times100$	$15\times15\times100$
Space group	$P4_32_12$	$P4_32_12$	$P4_32_12$	$P4_32_12$
a ($\mathring{A}$)	34.1 ± 0.1	34.1 ± 0.1	33.9	33.9
b ($\mathring{A}$)	34.1 ± 0.1	34.1 ± 0.1	33.9	33.9
c ($\mathring{A}$)	74.5 ± 0.1	74.5 ± 0.1	74.6	74.9
α, β, γ (°)	90.0, 90.0, 90.0	90.0, 90.0, 90.0	90.0, 90.0, 90.0	90.0, 90.0, 90.0
Resolution ($\mathring{A}$)	31.03 - 2.0 (2.1 - 2.0)	31.03 - 2.1 (2.2 - 2.1)	30.90 – 2.0 (2.1 – 2.0)	30.90 – 2.1 (2.2 – 2.1)
Dose (GGy)	~30	~20	$0.5\cdot10^{-3}$	$2.3\cdot10^{-4}$
Statistics				
Total # observations	2281705 (82905)	840310 (23885)	101998 (12279)	87801 (8364)
Number of hits	29586	11897	-	-
Indexed patterns	21706	9336	-	-
Indexing rate (%)	73.4	78.5	-	-
Multiplicity	398.5 (147.5)	170.8 (57.6)	18.2 (16.3)	18.0 (13.5)
Unique reflections	5717 (562)	4857 (415)	5611 (754)	4864 (621)
Completeness (%)	99.94 (99.47)	98.3 (85.57)	100.0 (100.0)	100.0 (100.0)
$I/\sigma(I)$	8.74 (2.27)	5.45 (0.52)	31.44 (13.93)	30.50 (12.59)
R_{split} (%)**	19.43 (62.02)	32.24 (101.38)	-	-
$CC_{1/2}$ (%)	82.26 (29.07)	73.21 (27.80)	99.90 (99.50)	99.90 (99.00)
CC^* (%)	93.47 (67.12)	90.40 (66.00)	-	-
CC_{ano} (%)	18.67 (0.00)	-	92.00 (80.00)	-
Wilson B ($\mathring{A}^2$)***	3.8	15.8	12.3	14.1

* Standard deviation of the X-ray pulse duration was estimated from measured electron bunch lengths.

$$** \; R_{split} = \frac{1}{\sqrt{2}} \cdot \frac{\sum_{hkl} \left| I_{hkl}^{even\_images} - I_{hkl}^{odd\_images} \right|}{\sum_{hkl} \frac{1}{2}\left(I_{hkl}^{even\_images} + I_{hkl}^{odd\_images} \right)}$$

*** calculated by TRUNCATE

Figure 1 $2mF_{obs} - DF_{calc}$ (blue, 1.0 σ) and $F_{obs} - DF_{calc}$ (green, 2.5 σ) maps obtained from 10 cycles of "restrained refinement in Refmac5, coordinates of the 4Fe-4S clusters were removed from the model for (a,b) 7.36 keV and (c,d) 6.86 keV LCLS data sets. The 4Fe-4S clusters were superposed for the reference of the original positions of Fe and S atoms in the clusters.
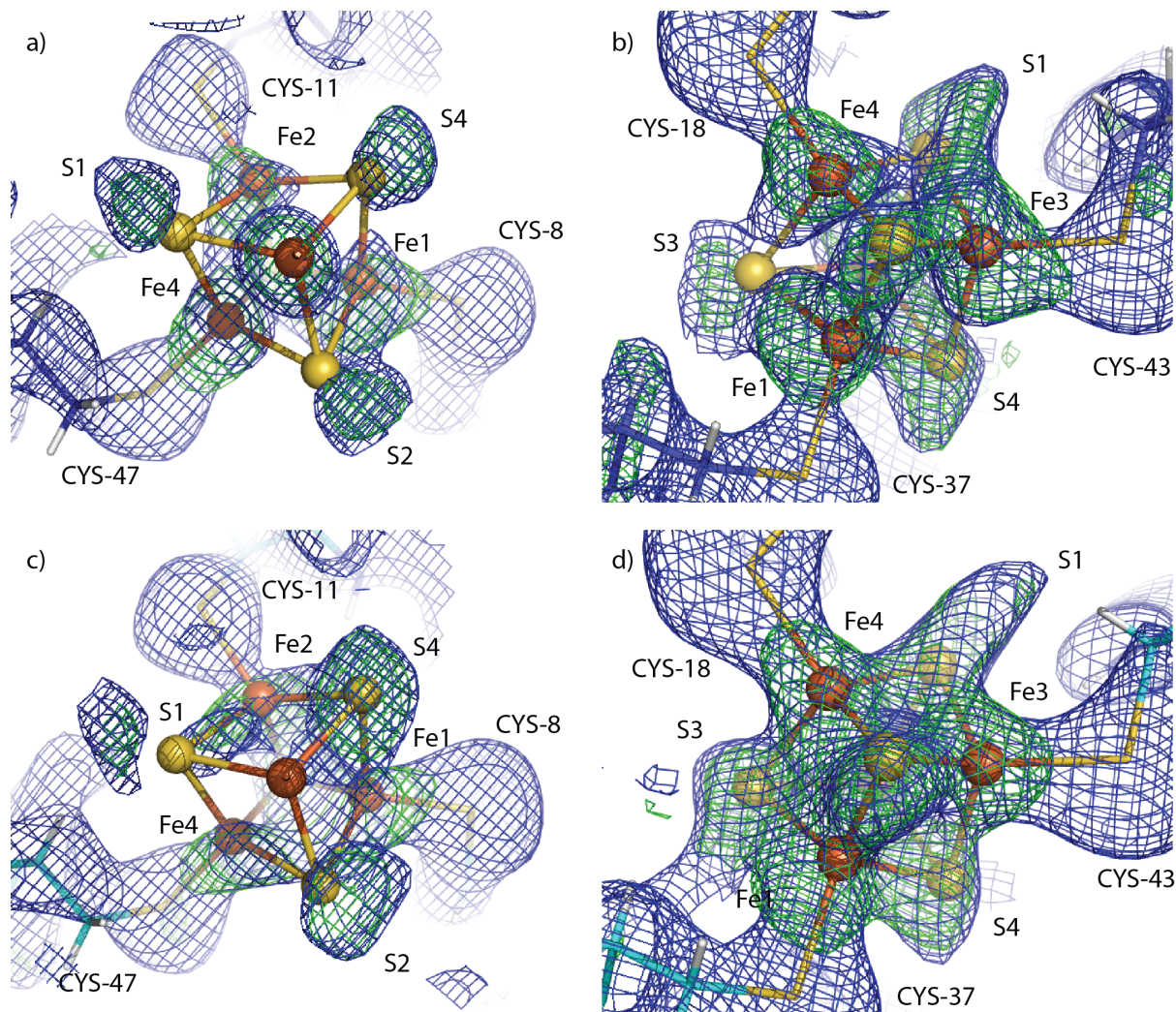
Figure 2 $2mF_{obs} - DF_{calc}$ (blue, 1.0 σ) and $F_{obs}-DF_{calc}$ (green, 2.5 σ) maps obtained from 10 cycles of "restrained refinement" in Refmac5, coordinates of the 4Fe-4S clusters were removed from the model for (a,b) 7.36 keV and (c,d) 6.86 keV SLS data sets. The 4Fe-4S clusters were superposed for the reference of the original positions of Fe and S atoms in the clusters.
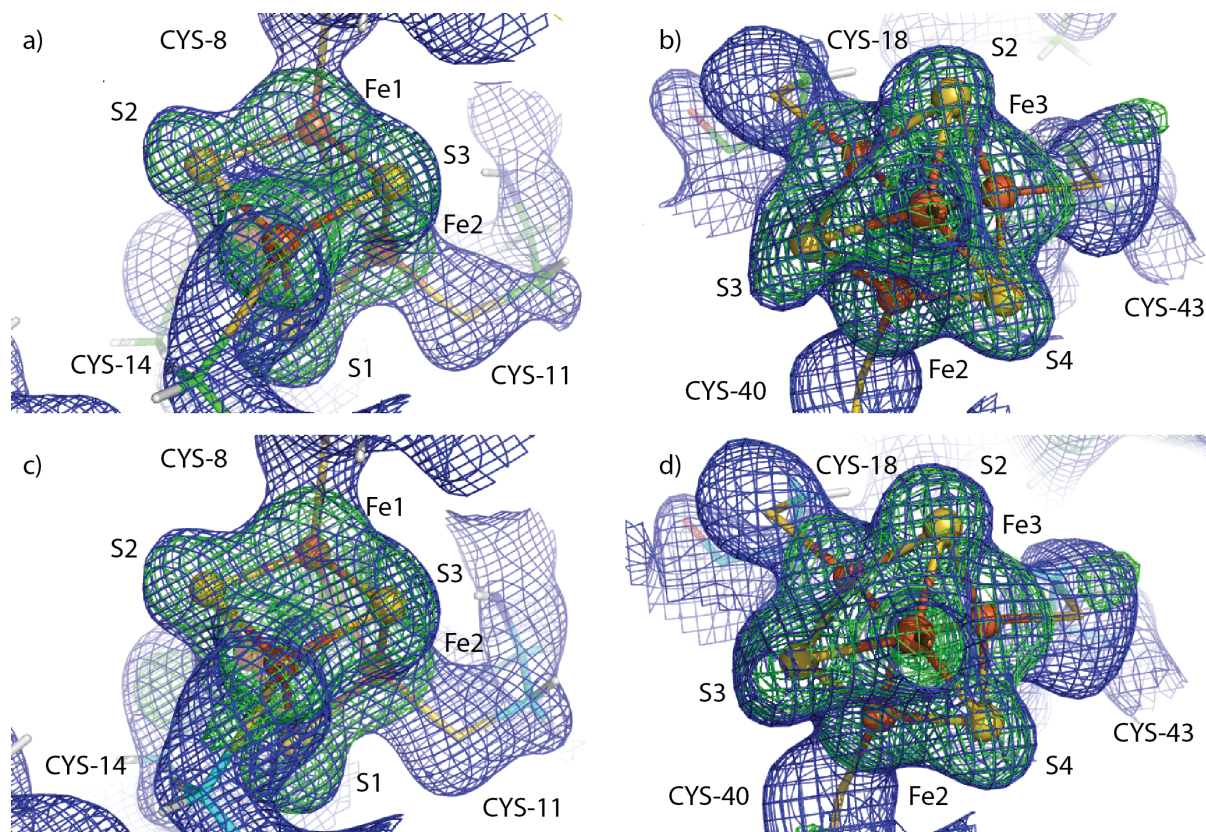
Figure 3 Ionization dynamics simulated with a plasma code. (a) Average ionization per atom for C, S and Fe, as a function of time during the pulse, for two photon energies (6.86 keV and 7.36 keV). Ionization saturates faster for light atoms and for Fe is dominated by collisional ionization. (b) Scattering power for C, S and Fe ions as a function of time, estimated from the number of bound electrons (without atomic form factors). (c) Expected accumulated signal during the pulse due to the loss of scattering power for C, S and Fe ions, compared to the neutral atoms, undamaged (black dashed line). (d) Calculated absorbed dose rate (MGy/fs) in the sample as a function of time, for two photon energies. The dose rate decreases during exposure due to saturation in ionization. (e) Absorption coefficient for Fe and S in the sample as a function of time. The drastic change in absorption for Fe above the K-edge in the first 20 fs due to a rapid loss of electrons and a continuum lowering in the plasma environment. .
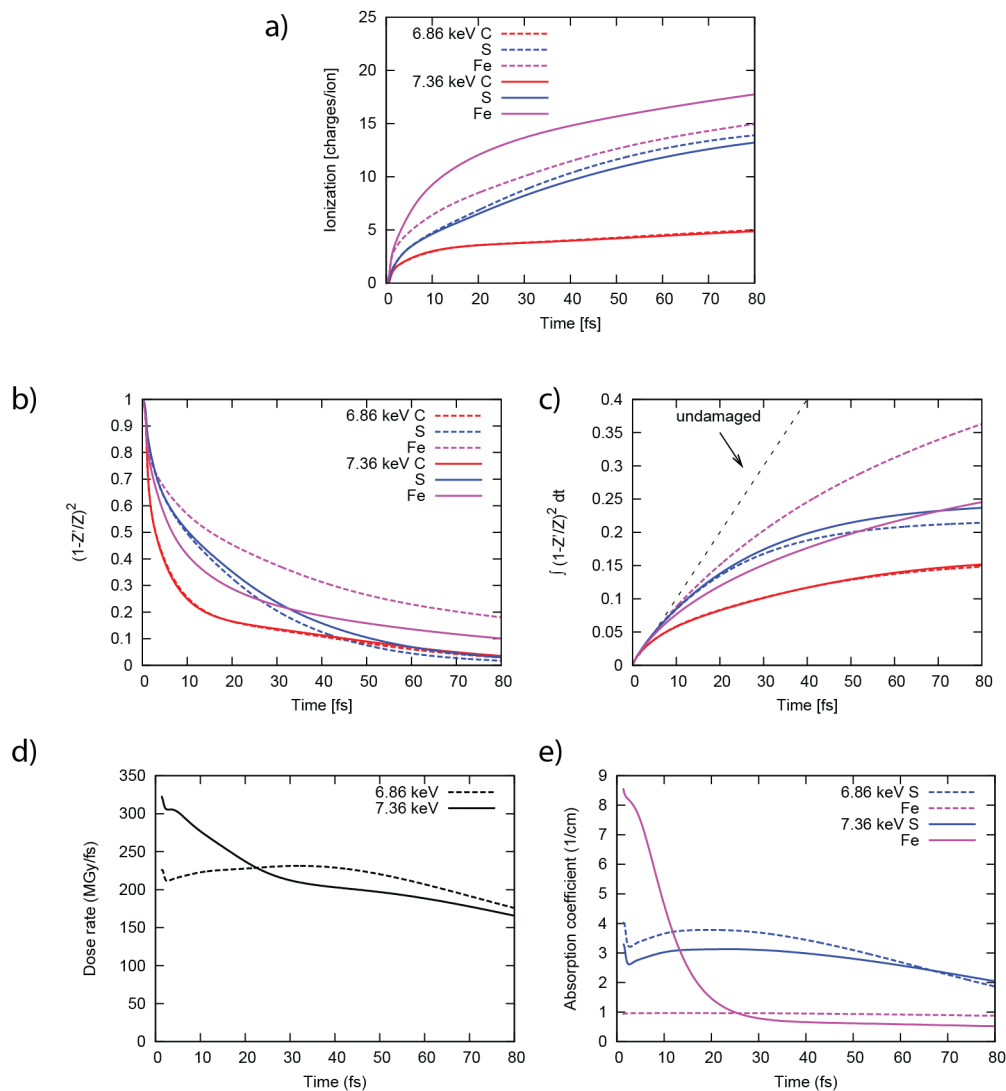
Supporting information

Figure S1 a) Image of the crystal suspension and b) size distributions for the crystal lengths and widths obtained from 222 and 196 measurements respectively. With fitted bell curves. The mean and standard deviations are reported in the legends. Measurements were performed using *AnalyzingDigitalImages* software obtained from:

https://sites.google.com/a/globalsystemsscience.org/global-systems-science/software/download
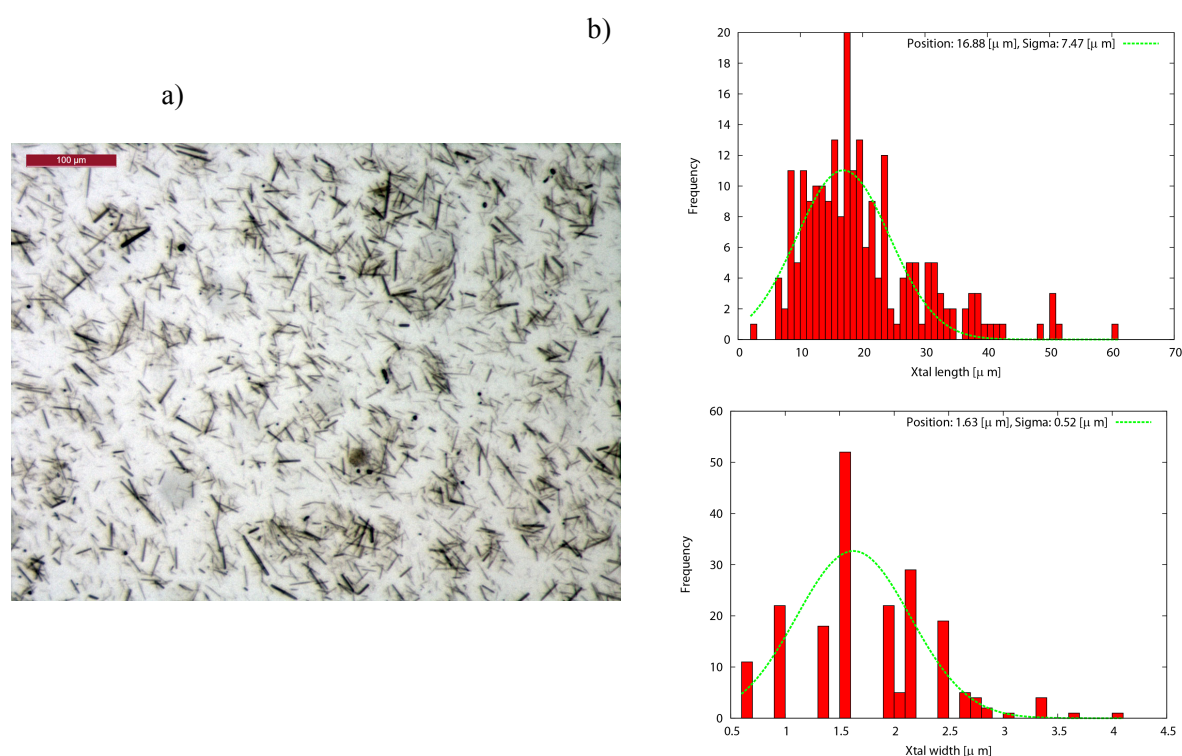
Figure S2 Construction of the post-sample attenuation filter. A sandwich of two filters was used. a) Transmittance of both filters at different positions, measured as function of the photon energy at the PTB FCM beamline. b,c) Mapping of the transmittance for both filters at 6.8 keV.

a)
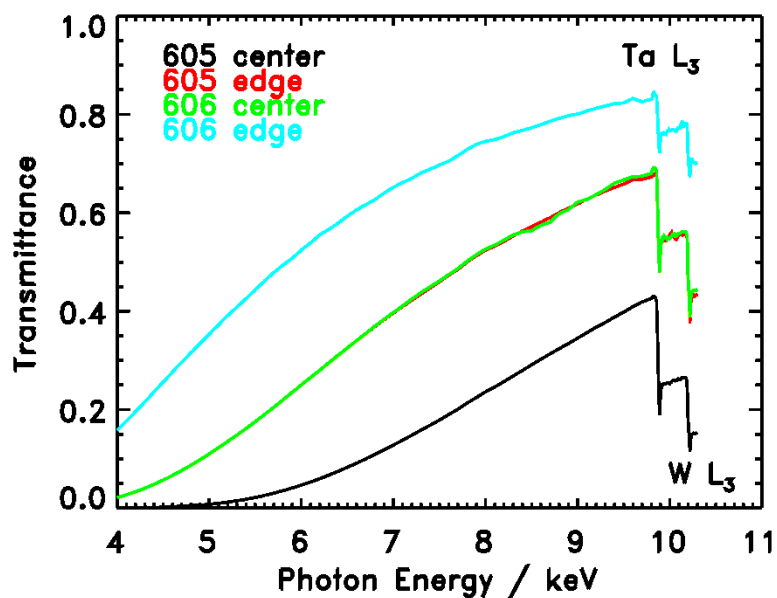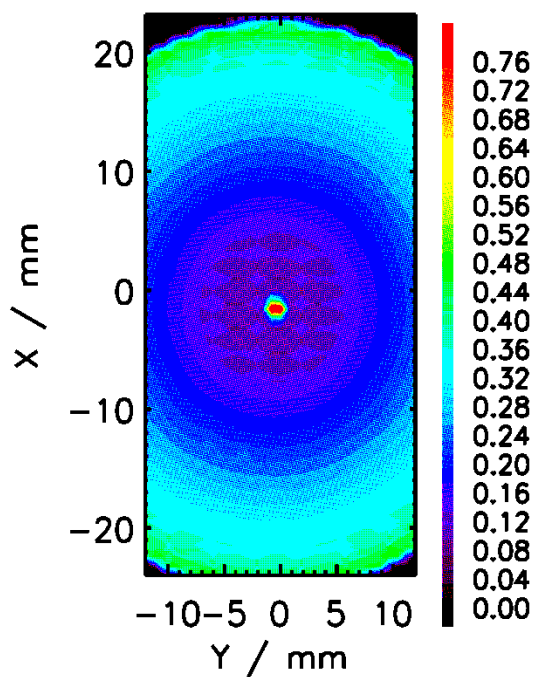
b)   c)

Figure S3 Distributions of a,b,c unit cell lenghts obtained from the ferredoxin 7.36 keV data set from a subset of 3500 randomly selected images indexed without cell reduction option in CrystFEL.
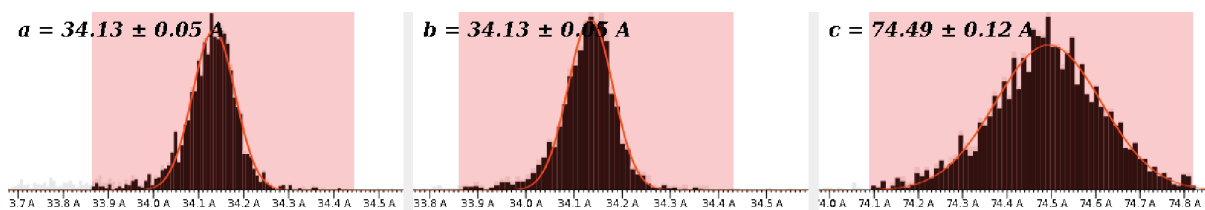
Figure S4 Wilson and cumulative intensity distribution plots for a) LCLS and b) SLS data sets.
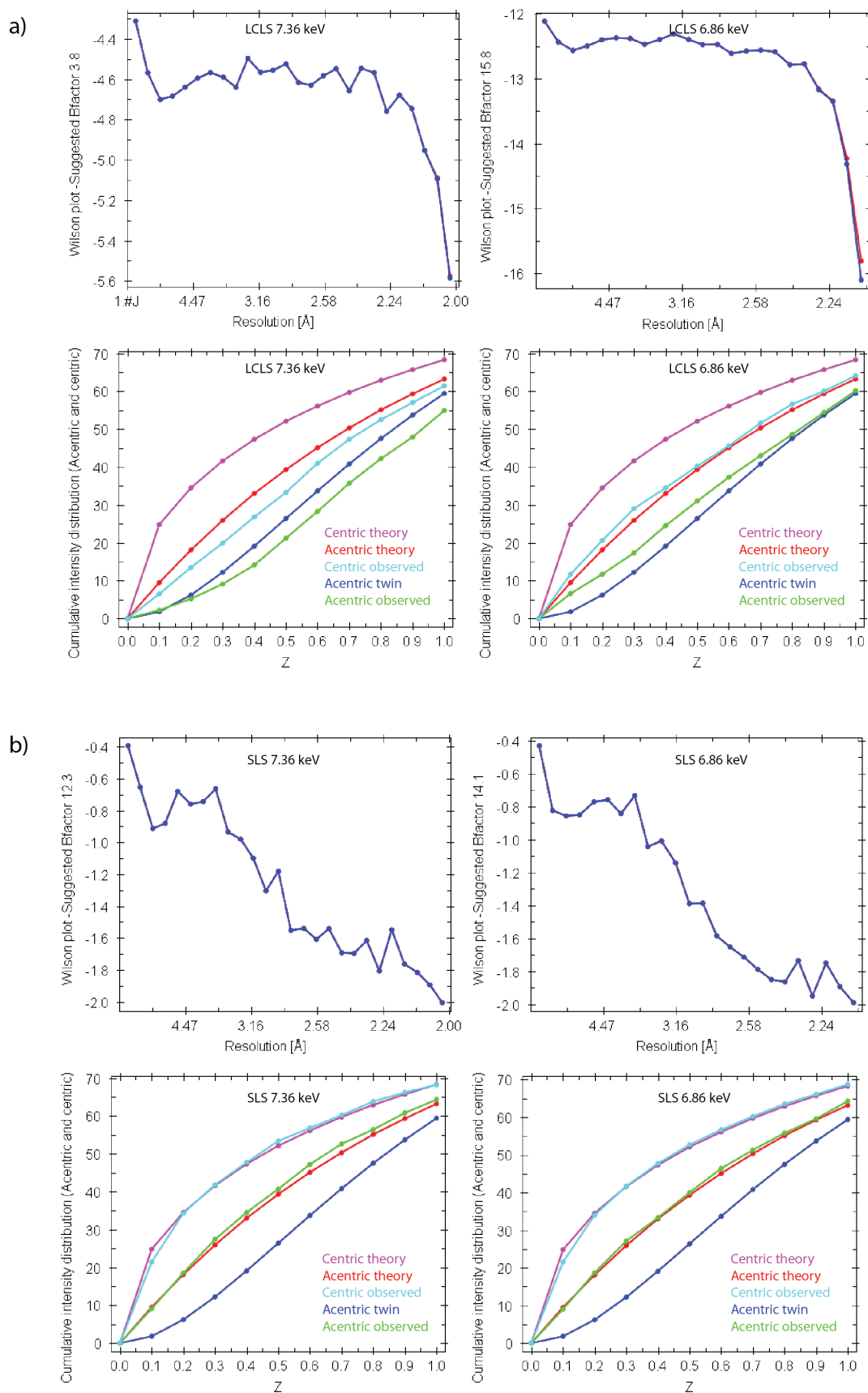
Figure S5 a) Ratios between calculated ferredoxin structure factors using model with the coordinates of the two [4Fe-4S] clusters included that are 10 or more times greater in magnitude than calculated ferredoxin structure factors using model without the coordinates of 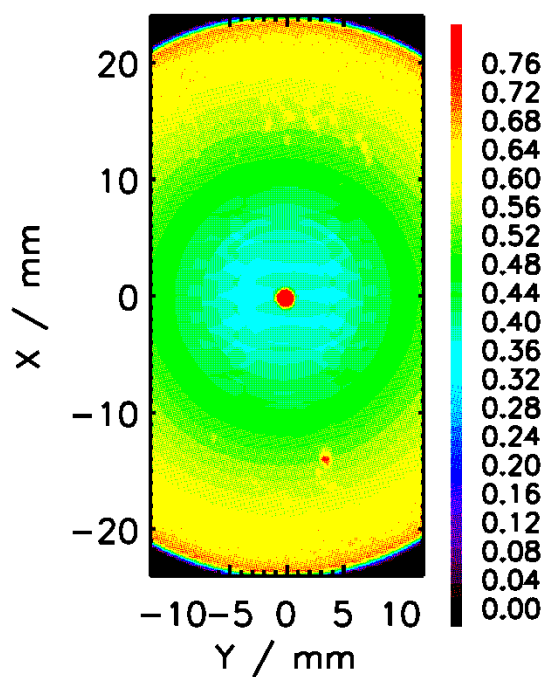the two [4Fe-4S] clusters (red). Ratios between structure factors measured at the synchrotron and at the LCLS at 7.36 keV (green). Ratios of the two ratios (blue).
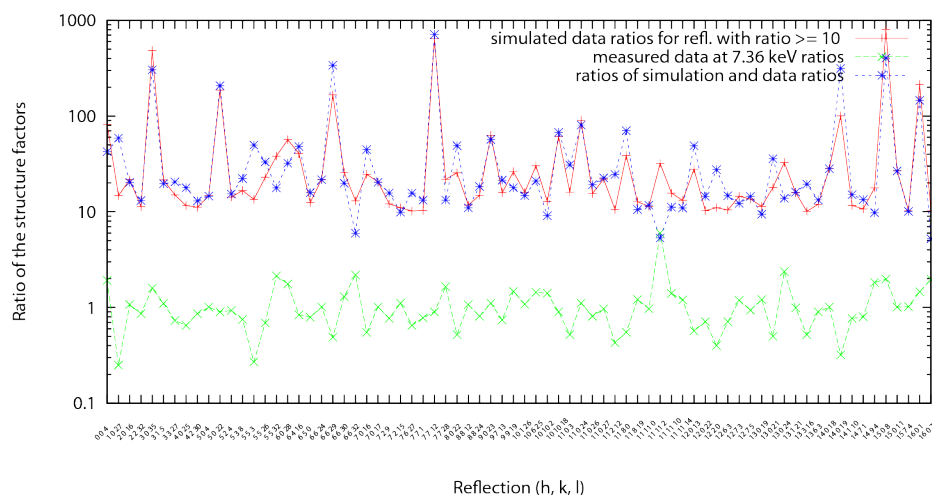
b) Ratios between calculated ferredoxin structure factors usind model with the coordinates of the two [4Fe-4S] clusters included and without the coordinates of the two [4Fe-4S] clusters, chosen at random (red). Ratios between structure factors measured at the synchrotron and at the LCLS at 7.36 keV (green). Ratios of the two ratios (blue).
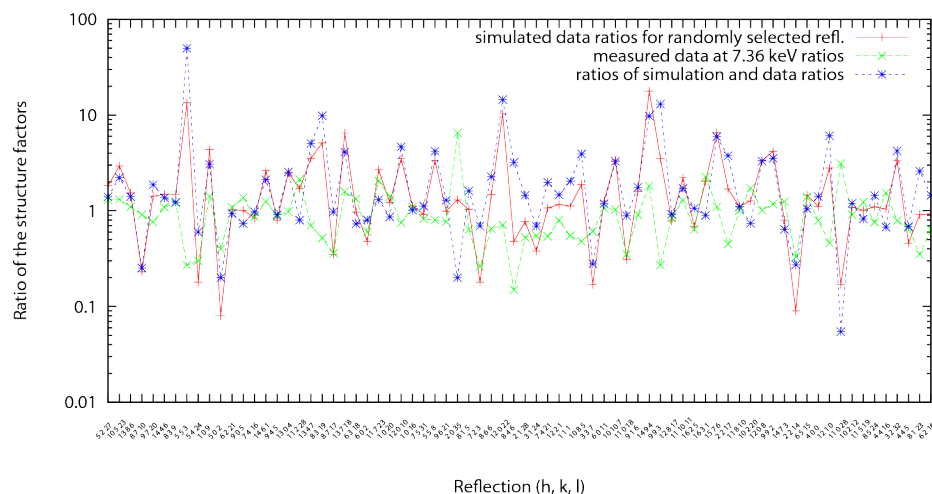
Figure S6 Simulation of Bragg termination. Wilson plots and cumulative intensity distributions for unaltered synchrotron data (a,b) as well as for the same data modified according to formula 3 from Barty et al. assuming 10 Å (c, d) and 40 Å atomic displacement at the end of the pulse. Neither the unusual Wilson plots, not the unusual cumulative intensity distributions observed for the LCLS ferredoxin data are not reproduced by Bragg termination alone. For 40 Å atomic displacement, the cumulative intensity distribution has even moved in the opposite direction of what is observed in the LCLS data.
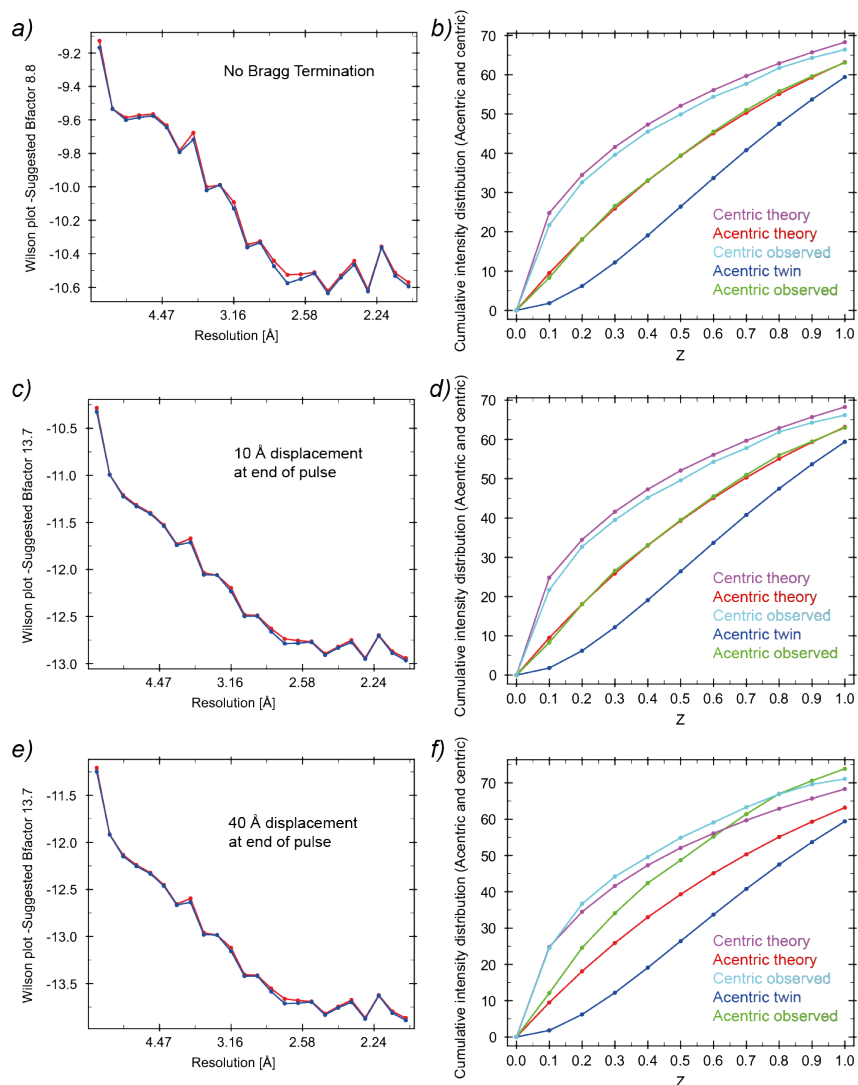
Figure S7 Simulation of Bragg termination with random local damage to different crystals reproduces the experimental intensity distribution.
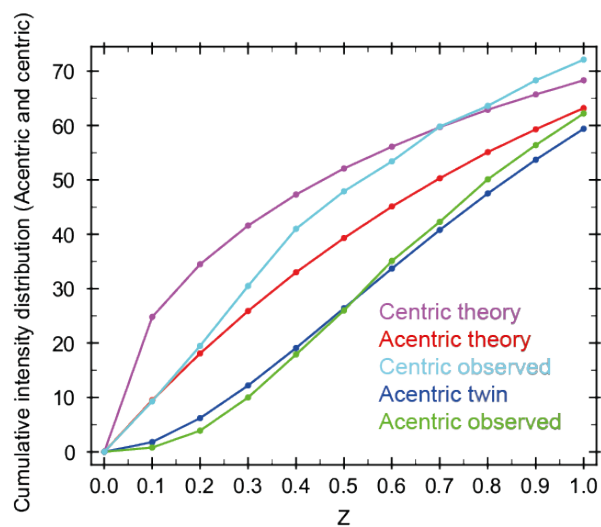
Figure S8 Information contents of the SLS and LCLS datasets. $2mF_{obs}$ - DF_{calc} map (1 σ, blue) F_{obs} - DF_{calc} (3 σ, green) electron density maps calculated after simulated annealing using PHENIX of the published ferredoxin model (2FDN, (Dauter *et al.*, 1997)) after removal of tyrosine 30, against the SLS (left) and LCLS data (right). Very little density for the missing residue (displayed for reference) returns in the LCPS maps, whereas it is very well defined in the SLS maps. The same feature is observed when omitting other amino acids.

SLS 7.36 keV   LCLS 7.36 keV
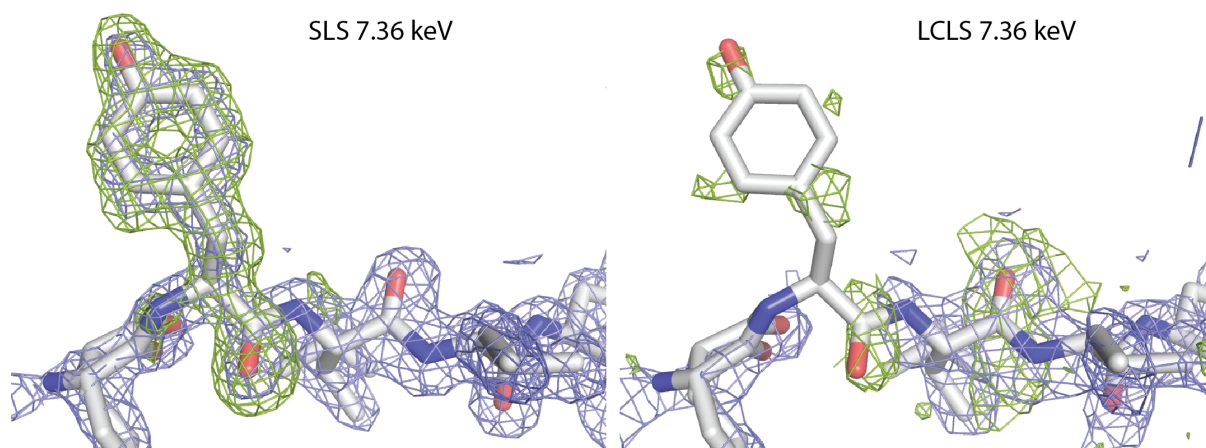
S1. Anomalous signal and phasing

Iron has a strong anomalous signal at 7.36 keV. We calculated phased anomalous difference Fourier maps from the LCLS data set. Fig. S9 shows the anomalous difference density peaks around iron atoms for the 7.36 keV LCLS data set contoured at 3σ and 5σ respectively. The heights of the anomalous peaks around Fe atoms in cluster 1 are lower than the peak heights in cluster 2 and differ between atoms within cluster 1.

Phasing of the 7.36 keV synchrotron data by the single wavelength anomalous diffraction (SAD) approach was straightforward using the program Phaser (McCoy *et al.*, 2007) followed by automatic model building using ARP/wARP. However, neither this approach nor a slightly modified version of the one described by Barends *et al.* for the *de-novo* phasing of SFX data of a lysozyme gadolinium derivative (Barends *et al.*, 2013) was successful for the ferredoxin SFX data. This is in line with the relatively low CC_{ano} (0.18) of the FEL data set. We next tried phasing by applying a single isomorphous replacement (SIR) approach, using the synchrotron data as native dataset and the 7.4 keV SFX data as derivative, analogously to a radiation damage-induced phasing (RIP) approach. However, also in this case it was not possible to phase the data, likely due to an apparent non-isomorphism of the two datasets caused by the unusual intensity distribution described in Section 3.1. Given the relative ease of phasing the synchrotron data based on the iron anomalous signal, and the difficulty in phasing the SFX structure using the same approach, it is possible that differences between the synchrotron and FEL structures can be attributed to a difference in the data quality of the two data sets, as indicated by the strength of the anomalous signal.

Figure S9   Phased anomalous difference Fourier map from LCLS data set contoured at 3 σ (a) and 5 σ (b). The heights of the peaks around Fe atoms are smaller in cluster I and not uniform within all Fe atoms in this cluster. At 5 σ contour level Fe3 atom in cluster I has no anomalous difference peak while other.
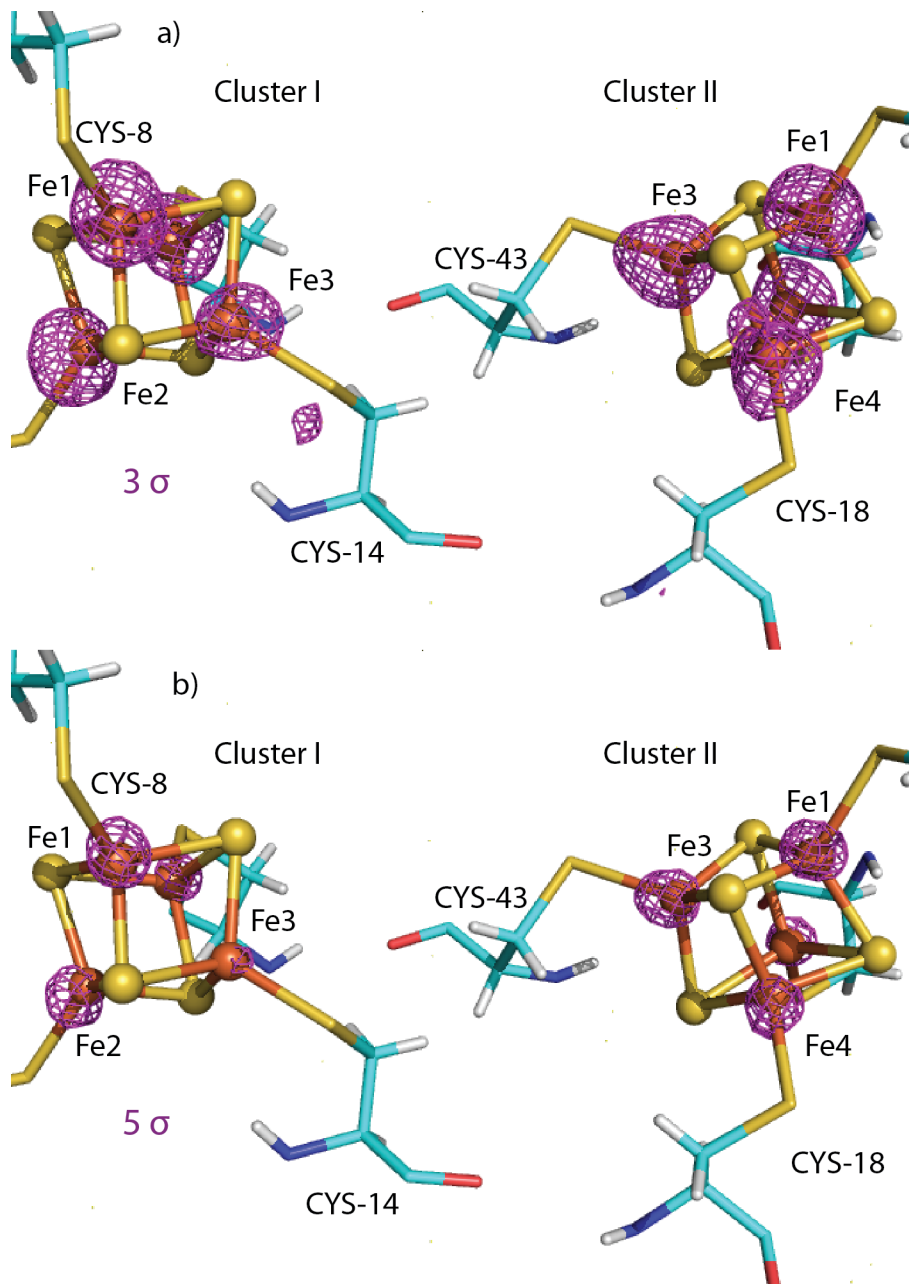
Figure S10 a) Difference maps between 7.4 keV LCLS and 6.9 keV LCLS data sets at ± 3 σ (green/red). No significant difference electron density is apparent around the cluster atoms. The sulphur atoms in the cysteine residues that hold the clusters in place have significant positive difference density. In particular residues number 8, 14, 37, 43. b) same view for corresponding maps for SLS data, show noise peaks not associated to atomic positions.
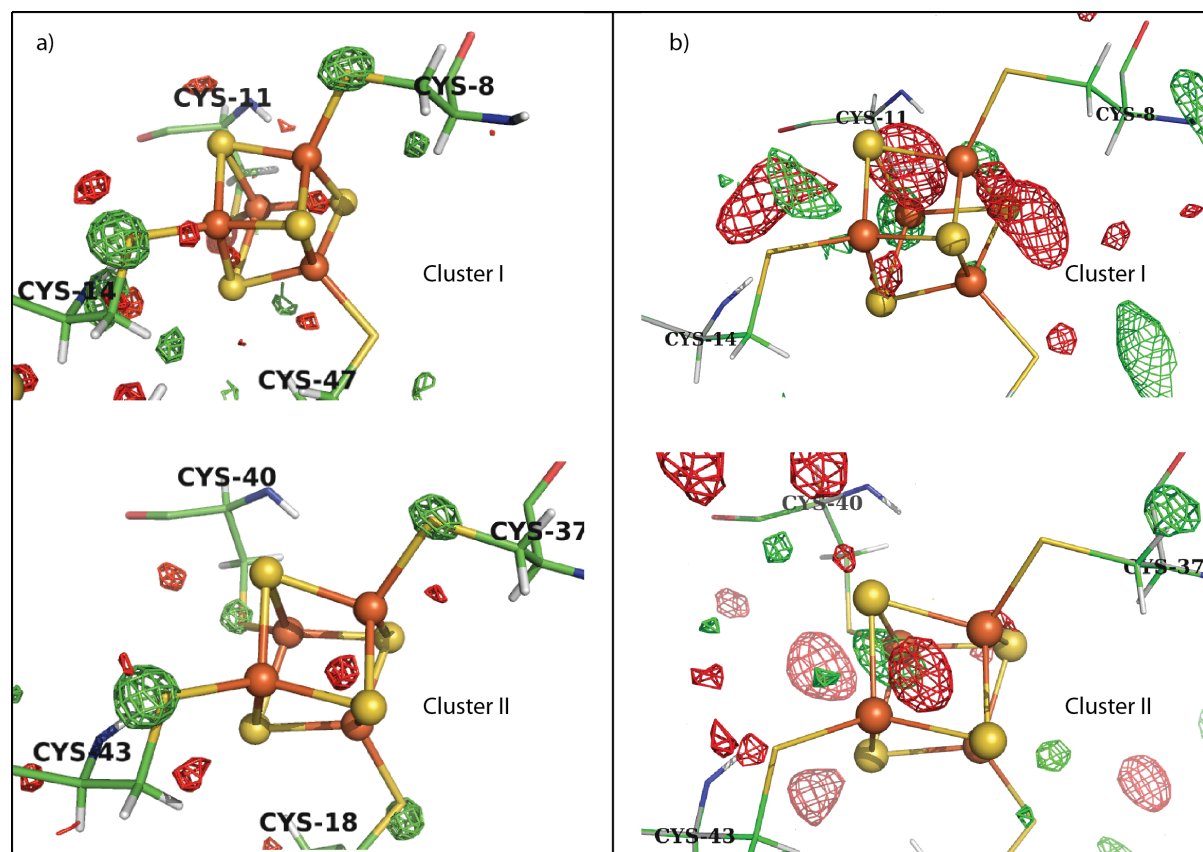
S2. Scaling

The LCLS and SLS data sets were scaled with XSCALE from XDS package. The summarized outputs from XSCALE and from the "Isomorphous difference map" tool in Phenix are given in the table S1. Numbers in parentheses refer to the highest resolution shell.

Table S1   Summarized scaling statistics.

SLS and LCLS data sets at	7.36 keV[1]	6.86 keV[1]
CC (XSCALE)	0.75	0.82
R-factor (XSCALE)	0.47 (0.73)	0.48 (1.19)
CC (PHENIX)	0.89 (0.55)	0.72 (0.43)
R-factor (PHENIX)	0.36 (0.41)	0.35 (0.63)

[1] Resolution range as mentioned in the table 1.

Table S2   R-FACTORS FOR INTENSITIES OF DATA SET LCLS 7.36 keV from XSCALE

RESOLUTION	R-FACTOR observed	R-FACTOR expected
10.00	58.1%	36.6%
8.00	48.4%	36.0%
7.00	48.8%	36.7%
6.00	44.2%	38.5%
4.50	39.7%	37.6%
4.00	42.0%	37.5%
3.50	43.1%	38.3%
3.00	40.3%	39.8%
2.50	44.0%	41.5%
2.30	45.3%	43.2%
2.20	49.5%	46.5%
2.10	46.9%	56.0%
2.00	72.9%	103.0%
total	46.6%	47.0%

Table S3   R-FACTORS FOR INTENSITIES OF DATA SET LCLS 6.86 keV from XSCALE

RESOLUTION	R-FACTOR observed	R-FACTOR expected
10.00	55.0%	37.9%
8.00	47.8%	37.9%
7.00	47.5%	38.3%
6.00	45.8%	44.9%
4.50	39.3%	38.8%
4.00	40.4%	39.2%
3.50	43.8%	41.1%
3.00	38.7%	40.4%
2.50	43.0%	43.2%
2.30	45.7%	47.0%
2.20	68.2%	70.9%
2.10	118.7%	114.8%
total	48.2%	47.3%

Table S4   Scaling statistics from the data sets at 7.36 keV from Phenix:

Bin#	Resolution range	Compl.	No.of refl.	CC	R factor
1:	30.8877 - 3.8239	1.00	526	0.891	0.2848
2:	3.8239 - 3.0360	1.00	468	0.840	0.2693
3:	3.0360 - 2.6525	1.00	467	0.791	0.2892
4:	2.6525 - 2.4101	1.00	456	0.755	0.3073
5:	2.4101 - 2.2374	1.00	461	0.749	0.2947
6:	2.2374 - 2.1055	1.00	438	0.750	0.2903
7:	2.1055 - 2.0001	1.00	446	0.553	0.4036

Table S5   Scaling statistics from the data sets at 6.86 keV from Phenix:

Bin#	Resolution range	Compl.	No.of refl.	CC	R factor
1:	30.9032 - 3.8140	0.98	529	0.870	0.2719
2:	3.8140 - 3.0281	0.98	481	0.806	0.2721
3:	3.0281 - 2.6456	0.98	464	0.789	0.2858
4:	2.6456 - 2.4038	0.98	461	0.767	0.2953
5:	2.4038 - 2.2315	0.98	463	0.651	0.3179
6:	2.2315 - 2.1000	0.98	397	0.434	0.6336

Table S6   Data statistics from CrystFEL for the LCLS 7.36 keV data set. a) R_{split}, b) CC, c) CC*, d) Rano/Rsplit e) CC_ano, f) Redundancy, SNR and other data statistics.

a)

Resolution shell centre (1/nm)	R_{split} (%)	# ref.	Resolution shell centre (Å)
1.295	7.80	585	7.72
2.623	8.85	567	3.81
3.136	10.70	586	3.19
3.516	11.40	573	2.84
3.827	13.33	567	2.61
4.093	13.55	578	2.44
4.328	14.35	559	2.31
4.541	19.16	570	2.20
4.735	33.13	569	2.11
4.914	62.02	533	2.04

b)

Resolution shell centre (1/nm)	CC	# ref.	Resolution shell centre (Å)
1.295	0.97113	585	7.72
2.623	0.96169	567	3.81
3.136	0.93454	586	3.19
3.516	0.92733	573	2.84
3.827	0.90447	567	2.61
4.093	0.92329	578	2.44
4.328	0.90125	559	2.31
4.541	0.87942	570	2.20
4.735	0.53172	569	2.11
4.914	0.29073	533	2.04

c)

Resolution shell centre (1/nm)	CC*	# ref.	Resolution shell centre (Å)
1.295	0.99265	585	7.72
2.623	0.99018	567	3.81
3.136	0.98293	586	3.19
3.516	0.98096	573	2.84
3.827	0.97459	567	2.61
4.093	0.97985	578	2.44
4.328	0.97368	559	2.31
4.541	0.96739	570	2.20
4.735	0.83323	569	2.11
4.914	0.67119	533	2.04

d)

Resolution shell centre (1/nm)	R_{ano} / R_{split}	# ref.	Resolution shell centre (Å)
1.503	1.46326	386	6.65
2.635	1.28121	444	3.79
3.143	1.33504	482	3.18
3.521	1.33955	486	2.84
3.830	1.39174	478	2.61
4.096	1.28597	496	2.44
4.330	1.19681	486	2.31
4.542	1.16798	498	2.20
4.735	1.12122	502	2.11
4.914	1.03139	462	2.04

e)

Resolution shell centre (1/nm)	CC_{ano}	# ref.	Resolution shell centre (Å)
1.503	0.31425	386	6.65
2.635	0.22138	444	3.79
3.143	0.27964	482	3.18
3.521	0.24415	486	2.84
3.830	0.22270	478	2.61
4.096	0.31139	496	2.44
4.330	0.19900	486	2.31
4.542	0.17169	498	2.20
4.735	-0.00699	502	2.11
4.914	-0.09042	462	2.04

f)

1/d (1/nm)	# ref.	Possible	Compl (%)	# Meas.	Red.	SNR	d (Å)
1.295	585	585	100.00	272675	466.1	15.50	7.72
2.623	567	567	100.00	271762	479.3	13.08	3.81
3.136	586	586	100.00	269278	459.5	11.40	3.19
3.516	573	573	100.00	277800	484.8	10.15	2.84
3.827	567	567	100.00	255837	451.2	8.79	2.61
4.093	578	578	100.00	268379	464.3	8.28	2.44
4.328	559	559	100.00	268399	480.1	7.79	2.31
4.541	570	570	100.00	197583	346.6	6.06	2.20
4.735	570	570	100.00	117087	205.4	4.09	2.11
4.914	562	565	99.47	82905	147.5	2.27	2.04

Table S7   Data statistics from CrystFEL for the LCLS 6.86 keV data set. a) R_split, b) CC, c) CC*, d) Redundancy, SNR and other data statistics

a)

Resolution shell centre (1/nm)	R_{split} (%)	# ref.	Resolution shell centre (Å)
1.240	11.08	501	8.06
2.499	14.40	502	4.00
2.987	14.20	487	3.35
3.349	18.01	487	2.99
3.644	20.84	500	2.74
3.898	21.44	495	2.57
4.122	26.70	497	2.43
4.325	37.84	476	2.31
4.509	56.53	439	2.22
4.680	101.38	343	2.14

b)

Resolution shell centre (1/nm)	CC	# ref.	Resolution shell centre (Å)
1.240	0.94665	501	8.06
2.499	0.88626	502	4.00
2.987	0.90317	487	3.35
3.349	0.85817	487	2.99
3.644	0.79086	500	2.74
3.898	0.83373	495	2.57
4.122	0.75911	497	2.43
4.325	0.53572	476	2.31
4.509	0.52997	439	2.22
4.680	0.27790	343	2.14

c)

Resolution shell centre (1/nm)	CC*	# ref.	Resolution shell centre (Å)
1.240	0.98620	501	8.06
2.499	0.96938	502	4.00
2.987	0.97422	487	3.35
3.349	0.96108	487	2.99
3.644	0.93980	500	2.74
3.898	0.95358	495	2.57
4.122	0.92901	497	2.43
4.325	0.83527	476	2.31
4.509	0.83233	439	2.22
4.680	0.65949	343	2.14

d)

1/d (1/nm)	# ref.	Possible	Compl (%)	# Meas.	Red.	SNR	d (Å)
1.239	506	506	100.00	106698	210.9	10.2	8.07
2.498	503	503	100.00	102345	203.5	8.53	4.00
2.987	487	487	100.00	102713	210.9	7.71	3.35
3.349	487	487	100.00	101649	208.7	6.68	2.99
3.644	500	500	100.00	97531	195.1	5.65	2.74
3.898	495	495	100.00	106837	215.8	5.25	2.57
4.122	498	498	100.00	98506	197.8	4.64	2.43
4.325	479	479	100.00	62053	129.5	3.35	2.31
4.509	487	500	97.40	38093	78.2	1.97	2.22
4.680	415	485	85.57	23885	57.6	0.52	2.14